Absolute calibration of ribosome profiling assesses the dynamics of ribosomal flux on transcripts

Kotaro Tomuro[1,2,7], Mari Mito[1,7], Takahito Miyake[3], Siu Yu A. Chow[4], Masao Doi[3], Yoshiho Ikeuchi[4,5,6], Yuichi Shichino[1,*], and Shintaro Iwasaki[1,2,8,*]

[1]RNA Systems Biochemistry Laboratory, RIKEN Cluster for Pioneering Research, Wako, Saitama 351-0198, Japan

[2]Department of Computational Biology and Medical Sciences, Graduate School of Frontier Sciences, The University of Tokyo, Kashiwa, Chiba 277-8561, Japan

[3]Department of Systems Biology, Graduate School of Pharmaceutical Sciences, Kyoto University, Sakyō-ku, Kyoto 606-8501, Japan

[4]Institute of Industrial Science, The University of Tokyo, Meguro-ku, Tokyo 153-8505, Japan

[5]Department of Chemistry and Biotechnology, School of Engineering, The University of Tokyo, Bunkyo-ku, Tokyo 113-0033, Japan

[6]Institute for AI and Beyond, The University of Tokyo, Bunkyo-ku, Tokyo 113-0033, Japan

[7]These authors contributed equally.

[8]Lead contact

[*]Correspondence: yuichi.shichino@riken.jp (Y.S.), shintaro.iwasaki@riken.jp (S.I.)

Abstract

Ribosome profiling, which is based on deep sequencing of ribosome footprints, has served as a powerful tool to unveil the regulatory mechanism of protein synthesis. However, the current method has substantial issues: contamination by rRNAs and the lack of appropriate means to determine overall ribosome numbers in transcripts. Here, we overcome these hurdles through the development of "Ribo-FilterOut", which is based on the separation of footprints from ribosome subunits by ultrafiltration, and "Ribo-Calibration", which relies on external spike-ins of stoichiometry-defined mRNA-ribosome complexes. A combination of these approaches measures the absolute numbers of ribosomes on transcripts, the translation initiation rate, and the numbers of translation events on a transcript before its decay, all in a genome-wide manner. Moreover, our method revealed the allocations of ribosomes under heat shock stress, during aging, and across cell types. Our strategy transforms the ribosome profiling technique from relative to absolute quantification of translation.

Introduction

Translation is subjected to tight regulation to define the protein abundance in cells. Translational control copes with intra- and extracellular environmental changes. To survey the protein synthesis dynamics in cells, ribosome profiling (or Ribo-Seq) has been developed [1] and applied to a wide range of biological contexts [2–5]. This methodology is based on the RNase protection of the mRNA by ribosomes [6–8]. The deep sequencing of "ribosome footprints" unveils the positions of ribosomes across the transcriptome at codon resolution, providing a snapshot of the translation status in cells. Since its exploitation, ribosome profiling has revolutionized our view of protein synthesis. However, there is still room for technical improvement to break through the inherent issues in this approach.

A barrier in ribosome profiling experiments has been the extensive contamination of ribosomal RNA (rRNA) fragments that overwhelm the sequencing space. To suppress them, hybridization to biotin-labeled oligonucleotides and subsequent immobilization on streptavidin beads [9–14] and nuclease-mediated degradation by RNaseH [15,16] or duplex-specific nuclease (DSN) [17] have been used. In addition to direct rRNA fragment targeting, a reduction of the unwanted reads can be achieved after DNA library generation through Cas9-mediated degradation [12,18–20]. Even with such extensive efforts, there is much room to improve rRNA depletion in ribosome profiling.

Another challenge in ribosome profiling is global quantification. While deep sequencing-based analysis can assess relative changes, it is difficult to accurately follow global unidirectional changes in translation in ribosome profiling [21–23]. To remedy this issue, the supplementation of external standards or "spike-ins" has been employed; the addition of short synthetic oligonucleotides after RNase digestion [24–27] or the lysate from

an orthogonal species before RNase digestion [28–31] has been used for normalization. Similarly, footprints generated by mitochondrial ribosomes could be used for internal spike-ins when translation within organelles is reasonably assumed to be unaffected [32–36]. However, these methods cannot address the basic question of how many ribosomes are on each transcript, which hampers the kinetic and stoichiometric understanding of translation in cells.

To overcome these intrinsic difficulties, we developed two key techniques: Ribo-FilterOut and Ribo-Calibration. Ribo-FilterOut uses ultrafiltration to separate the ribosome footprints from large and small subunits of ribosomes after RNase treatment, deplete the fragmented but still complex-assembled rRNAs, and substantially increase usable sequencing space for ribosome footprints. Ribo-Calibration employs spike-ins of mol ratio-defined ribosomes associated with mRNA prepared by an *in vitro* translation system; the supplementation of the complex assesses the ribosome numbers on transcripts by data standardization. In combination with other comprehensive techniques, such as ribosome run-off assays and mRNA half-life measurements, Ribo-Calibration revealed the translation initiation speed and number of translation rounds before mRNA decay across the transcriptome. We found that various cellular conditions, including heat shock stress, tissue aging, and cell type differences, may alter the allocation of ribosomes globally and/or in an mRNA-specific manner. By reducing unwanted RNA fragments, our approaches provide a versatile platform for absolute quantification of the protein synthesis rate.

Results

Separation of ribosome subunits and footprints allows efficient depletion of rRNA in ribosome profiling

An issue in ribosome profiling has been contamination by rRNAs, which overpopulates the sequencing libraries and thus reduces the sequencing space for ribosome footprints. For example, in the experiment with HEK293 cells, 92% of reads were reads from rRNA [9.2×10^5 reads per million (RPM)], and only 5.4% (0.54×10^5 RPM) of reads were available for downstream analysis (Figure 1B). Thus, rRNA subtraction by hybridizing oligonucleotides tethered to magnetic beads (such as Ribo-Zero from Illumina) has typically been included in the process of library preparation [9–14] (Figure 1A). This approach reduced rRNA contamination (to 76%) and increased the yield of usable reads (18%) in the library (Figure 1B). However, a large fraction of rRNAs still escaped subtraction. Thus, an orthogonal approach was required to improve the output of ribosome profiling.

Here, we modified the protocol to physically dissociate the ribosome footprints from ribosomes (Figure 1A). In the standard method, ribosomes holding the footprints were sedimented by sucrose cushion ultracentrifugation, and then the RNA constituents in the pellet were directly purified. Instead, in the modified protocol the ribosome pellet was suspended in a buffer containing EDTA, which splits the ribosomes into subunits and released footprints from the complex (Figure 1A). The detached footprints were separated from ribosome subunits based on molecular sizes; the ultrafiltration filter could pass the small footprints but not the macromolecular ribosome subunits with rRNAs. Indeed, this procedure—termed "Ribo-FilterOut"—eliminated a large amount of RNA fragments, which most likely originate from rRNAs (Figure S1A and S1B). The remaining ~30-

nucleotide (nt)-long fragments were expected to be ribosome footprints since they disappeared upon EDTA pretreatment, which excludes mRNA from ribosomal protection against RNase digestion (Figure S1A and S1B).

The application of Ribo-FilterOut improved the performance of ribosome profiling. Ribo-FilterOut increased the usable reads (21% in the library) (Figure 1B). Moreover, the combination of Ribo-FilterOut with rRNA subtraction by hybridizing oligonucleotides (Ribo-Zero) showed even higher yields of ribosome footprints (49% in the library) (Figure 1B), indicating that the application of two different rationales has additive impacts.

Ribosome profiling prepared with Ribo-FilterOut can monitor the translatome with limited biases. We observed the high quality of footprints in Ribo-FilterOut-applied samples: footprint length peaked at 30 and 22 nt (Figure S1C) [37,38] and the 3-nt periodicity along the open reading frame (ORF) (Figure S1D). Strikingly, the reads mapped to the CDS showed high reproducibility between replicates and among the different options for rRNA depletion (Figure 1C).

We applied the same strategy to ribosome profiling from other model organisms, such as *D. melanogaster*, *S. cerevisiae*, *A. thaliana*, and *E. coli*. Although the impact of Ribo-FilterOut varied across species, overall, the combination of Ribo-FilterOut and rRNA subtraction methods provided the highest recovery of usable reads in the libraries (Figure S2A-D), except for yeasts. Thus, the Ribo-FilterOut approach using biochemical separation of footprints from ribosomes was an easily implemented option for high-yield ribosome profiling in many species.

Purified mRNA-ribosome complex spike-in measures the global shift of protein synthesis in ribosome profiling

Another challenge in ribosome profiling is to reflect global changes in the protein synthesis rate. To calibrate ribosome profiling data to measure the net alteration of translation, we used the purified mRNA-ribosome complex with known molarity as the normalization spike-in (termed Ribo-Calibration). The addition of this spike-in to the lysate even before RNase digestion allowed subsequent library preparation procedures without any modification. For this purpose, we harnessed the *in vitro* translation system with rabbit reticulocyte lysate (RRL); mRNAs encoding *Renilla* and firefly luciferases (Rluc and Fluc) were subjected to translation *in vitro,* and then the complex with two (for Rluc) or three (for Fluc) ribosomes was isolated by sucrose density gradation and ultracentrifugation (Figures 2A and S3A). Indeed, the addition of the mRNA-ribosome complexes to HEK293 T-REx cell lysate in ribosome profiling captured the footprints across the Rluc and Fluc ORFs (Figure S3B) with high 3-nt periodicity, as in cellular transcripts (Figure S3C).

To test the utility of this spike-in for monitoring global translation, we induced translation repression with Rocaglamide A (RocA), a translation inhibitor that targets eukaryotic translation initiation factor (eIF) 4A [32,34,35,39–41]. In earlier studies [32,34,35], ribosome profiling data were normalized to mitochondrial ribosome (mitoribosome) footprints used as internal spike-ins, assuming that RocA should not cause any translation change in the mitochondria. We observed similar calibration outcomes with the supplemented spike-ins (Figure 2B and 2C) to those obtained with mitoribosome footprints (Figure S3D) in a RocA dose-dependent manner. Simultaneous RNA-Seq from the same material and the subsequent data calibration showed no significant alteration in

the overall RNA abundance (Figure 2D and 2E), ensuring that footprint reduction with RocA stems from the impact on translation. These data indicated the potential of Ribo-Calibration for data normalization when global protein synthesis is attenuated.

Ribo-Calibration estimated the absolute number of ribosomes per mRNA across the transcriptome

After data normalization by Ribo-Calibration, we could determine the absolute number of ribosomes per mRNA. Specifically, we assessed the ribosome numbers on each mRNA by determining the stoichiometry between ribosomes and luciferase mRNAs (Figure 3A, see Experimental procedures for details). The observed ribosome numbers on Rluc and Fluc used for Ribo-Calibration ensured the accuracy of this measurement (Figure 3B).

We applied this calculation across the transcriptome and found a diversity of ribosome numbers on mRNAs, with 5.09 ribosomes on average (Figure 3C and Table S1). As expected, longer ORFs had a higher number of ribosomes (Figure 3D and Table S1). Based on the ORF length, the average distance between ribosomes on the transcripts was calculated to be 269 nt (Figure 3E).

RocA treatment also confirmed the validity of this ribosome molarity calculation. Globally, RocA reduced the number of ribosomes in a dose-dependent manner (Figure S4A). As expected, RocA greatly increased the distance between ribosomes (Figure S4B). Simultaneously, RocA showed selectivity in repressing a subset of mRNAs [32,34,35,39–41] (Figure S4C). The ribosome numbers on high-sensitivity mRNAs were dramatically reduced by RocA, whereas those on low-sensitivity mRNAs were completely resistant (Figure S4D). Thus, the absolute ribosome number calibration accurately revealed the ribosome loading rate across transcripts.

mRNAs with tightly packed ribosomes

We noticed that a subset of mRNA showed an extremely short distance between ribosomes: ~30 nt, the same length of mRNA occupied by a ribosome (Figure 3E inset). These "tightly packed" mRNAs were associated with gene categories related to the translation machinery, which requires high expression for active cell growth (Figure 3F).

Given this high density of ribosomes on ORFs, we wondered whether this may cause ribosome collision. However, the comparison of disome profiling, which captures long footprints generated by two consecutive ribosomes [19,27,42,43], revealed that the ribosome-packed mRNAs were not significantly associated with ribosome collision (Figure S4E). Thus, although highly ribosome-loaded mRNA may have a stochastic bump of ribosomes, this may not cause stable ribosome traffic jams that evade the induction of ribosome-associated quality control [44,45].

The absolute number of ribosomes per codon

In addition to mRNA-wise measurements, our method determined the absolute ribosome numbers on each codon. This analysis could assess the ribosome presence probability in terms of mRNA codons; the averaged ribosome probability along ORFs revealed that the start codons may be occupied by ribosomes at ~6% probability and the stop codons at ~12.5% probability (Figure 3G).

Our mRNA-centric analysis for ribosome probability led us to revisit the known translation-attenuating codons. *XBP1u* mRNA [19,46–48] has been well recognized as a source of ribosome stalling. However, the pause site showed only ~24% occupancy (Figure S4F) due to the relatively low ribosome loading on the transcript (~1.76 ribosome

per mRNA). Recently, uORF0, which is composed of an ATG start codon and adjoined stop codon, in the 5′ UTR of *ATF4* mRNA, has been proposed to act as a physical roadblock to prevent ribosome load downstream [49]. In our analysis, ~21% of uORF0 was covered by ribosomes (Figure S4G), leaving the remaining ~79% of uORF0 free of ribosomes. Thus, Ribo-Calibration provided additional benefits in understanding the ribosome occupancy probability on mRNA.

Translation initiation as a global rate-limiting step

In combination with the ribosome elongation rate, Ribo-Calibration empirically defines the translation initiation rates across the cellular transcriptome. To measure ribosome traversal speed, we applied a ribosome run-off assay [47]; after blocking new ribosome loading onto mRNA by harringtonine (HAR), which inhibits the first round of elongation, preloaded ribosomes were chased and halted by cycloheximide (CHX) over time (Figure S5A). Ribosome profiling in these conditions generated a ribosome-free area downstream of the start codons and extended it over time (Figures 4A and S5A) [47]. The regression of the length of the ribosome-free region to the time revealed the elongation rate to be 4.08 codon/s in HEK293 T-REx cells (Figure 4B), a similar number to that measured with the same method in mouse ES cells [47] and tissues [50]. Given that the ribosome number per transcript is a function of the translation initiation rate, translation elongation rate, and ORF length (see Experimental procedures for details), the translation initiation rate was deduced to be 22.0 s/event on average, but with a wide variety across transcripts from ~3 s/event to ~80 s/event (Figure 4C and Table S1). A subset of mRNAs that are known to be translated well, such as those encoding translation machinery proteins, often possess

a 5′ terminal oligo pyrimidine (TOP) [51]. The higher rate of translation initiation for TOP mRNAs confirmed our measurements of translation kinetics (Figure 4D).

Lifetime rounds of translation on transcripts

Moreover, given the half-lives of mRNAs, the cycles of mRNA usage for translation could be evaluated. We estimated the mRNA decay rate by 5′-bromo-uridine immunoprecipitation chase–deep sequencing (BRIC-Seq) [52,53] (Figures 4E, S5B, and Table S1). Considering the probability of mRNA decay during 5 half-lives (when ~97% of the mRNA is decayed), mRNAs were expected to be used 1782 times before the decay on average (Figure 4F and Table S1). The lifetime translation events were highly mRNA dependent with a range of ~55-fold.

Thus, combined with other techniques, our Ribo-Calibration offered a versatile approach for estimating a variety of kinetic and stoichiometric information regarding ribosomal flux across transcriptomes (Figure 4G).

The quantification of ribosomal flux in heat shock stress

To evaluate the utility of Ribo-Calibration, we applied this method to translation alteration during physiological stresses. For this purpose, we subjected cells to heat shock, a well-recognized stress to reprogram translation [54,55] (Figure S6A). The effect of heat stress and the recovery process was verified using metabolic labeling of newly synthesized proteins using OP-Puro experiments and Western blot analysis for Hsp70 (Figure S6B and S6C). Ribo-Calibration was able to detect a global decrease in translation by heat shock peaking at the 1 h time point and its return to baseline levels during the recovery culture (Figures 5A and S6D), whereas mRNA abundance alteration was limited

(Figure 5B). Accordingly, the ribosome numbers on the transcript also followed the trends in global translation (Figures 5C and S6E). The extent of reduction in these data was also consistent with the OP-Puro experiments (Figure S6B).

Even under the global repression of protein synthesis, heat shock proteins have been thought to be preferentially translated to cope with stress [54,55]. However, the calibrated ribosome profiling data disproved this dogma; during heat shock, the protein synthesis of heat shock protein (Hsp) 70 was also attenuated (Figure 5D). Only in the recovery phase did Hsp70 translation exceed that in naïve cell status, concomitant with transcription induction (Figure 5E). Ultimately, the ribosome numbers on the Hsp70 transcripts did not surpass those observed in cells before heat shock (Figure 5F). Thus, Hsp70 expression under heat shock stress could be largely explained by transcriptional induction but not translational activation, at least in our conditions.

Another group of mRNAs that were expected to undergo active translation during heat shock consists of upstream open reading frame (uORF)-containing mRNAs. Heat shock entails the phosphorylation of eIF2α and the integrated stress response (ISR) [56], leading to global translation repression. Simultaneously, the ISR allows the activation of translation from a subset of mRNAs, including those possessing uORFs [25,56,57]. Among the representative uORF-containing mRNAs [25], we observed two types of responses during heat shock; translation was indeed "activated" with increased numbers of ribosomes per transcript (Figure 5G; exemplified by *ATF4* and *IFRD1*), whereas translation was relatively resistant to global translation reduction, that is, the ribosome numbers on the transcripts remained unchanged (Figure 5H; exemplified by *PPP1R15B* and *PTP4A1*).

In addition to this translation initiation regulation, earlier ribosome profiling studies have indicated ribosome stalling in the early elongation phase (~65 codons) in heat shock [54] or by the unavailability of Hsp70 [58]. Our data recapitulated the higher ribosome occupancy in that region by heat shock when the relative enrichments were considered (Figure S6F). However, the absolute calibration of ribosome numbers across CDS negated such a pileup, owing to the global reduction in ribosome loading across the transcriptome (Figure S6G).

Taking these data together, ribosome profiling with Ribo-Calibration provided an accurate view of protein synthesis in stress responses.

Ribosome flux differences among cell types

We further applied our approach to various cell types, including induced pluripotent stem (iPS) cells and skin cells (melanocytes, fibroblasts, and keratinocytes) (Figures 6A and S7A-E). We also extended this analysis to tissues from young (3 months) and old (24 months) mouse forebrains (Figures 6A and S8A-D). We observed differential ribosome numbers on transcripts across different cellular or tissue conditions (Figure 6A).

We noticed that skin cells led to high ribosome fluxes on a subset of mRNAs required for specialization of the cell [59,60]: *TYR*, *TYRP1*, and *DCT*, which encode enzymes required for melanin biosynthesis [61], in melanocytes; extracellular matrix protein lumican (LUM), which induces fibrocyte differentiation [62], in fibroblasts; and keratin (*KRT75*, *KRT6B*, *KRT6C*, *KRT16*, and *KRT15*) in keratinocytes (Figure 6B). In addition to genes that define the cell functions, differential ribosome loading on a subset of transcripts (here scored by the distance between ribosomes considering ORF length) was found (Figure S7F-L).

During our analysis of HEK293 cells for RocA-mediated translation repression (Figure 2) and heat shock response (Figure 5), we noticed that basal ribosome numbers on transcripts were very different and that this discrepancy may come from the source/strain of the cells [HEK293 T-REx (from Thermo Fisher Scientific), ~5.1 ribosomes; HEK293 (from American Type Culture Collection, ATCC), ~2.3 ribosomes] (Figure 6A). This difference in ribosome loading reflected the overall protein synthesis, probed by OP-puro (Figure 6C), and thus led to the growth rate variation (Figure 6D).

Therefore, our data indicated that the ribosome flux on individual mRNAs and that at the whole transcriptome level define cell function and cell proliferation.

The aged forebrain possesses a lower amount of mRNAs with a constant ribosome loading rate

Consistent with the idea of an aging-dependent reduction in global protein synthesis [63–65], we observed declines in overall translation in calibrated ribosome profiling (Figure 6E). However, this was not reflected in the ribosome numbers on transcripts (Figures 6A and S8B-D), since the mRNA abundance in the aged forebrain was also diminished (Figure 6F). Thus, the reduction in global protein synthesis in the aged forebrain was caused by decreased mRNA availability. Even without the overall alteration in ribosome loading, the distance between ribosomes on a subset of transcripts was changed during aging (Figures 6G and S8F-G), suggesting mRNA-selective dysregulation induced by aging.

Taken together, these data show that Ribo-Calibration transforms ribosome profiling experiments into a means to measure definite translation, with the aid of Ribo-FilterOut for increasing sequencing space.

Discussion

Here, we showed that the combination of Ribo-FilterOut with the hybridization of oligonucleotides and the subsequent rRNA fragment pullout (*i.e.*, Ribo-Zero) showed the best performance. In addition, a reduction in unwanted reads can be achieved after DNA library generation using Cas9-mediated degradation [12,18–20]. The application of this strategy may have the potential to further increase the sequencing depth for usable reads in ribosome profiling.

To quantify the global translation change in ribosome profiling data, short DNA or RNA oligonucleotides, corresponding to footprint size, have been used [24–27]. However, the addition of the oligonucleotides could only be possible in the middle of library preparation, such as after RNase digestion and footprint recovery from ribosomes, and we have to assume that no variance of samples occurs before spike-in supplementation. In contrast, spike-ins of lysate of orthogonal species or purified mRNA-ribosome complex (*i.e.*, Ribo-Calibration) can be introduced before RNase digestion, thus a more suitable approach for the calibration. Ribo-Calibration provides a further advantage for measuring absolute ribosome numbers on transcripts or codons.

Our estimation of the ribosome numbers on transcripts, the distance between ribosomes, and translation initiation rates aligned very well with those measured by single-molecule imaging for translation [66–72]. Instead of the artificial reporters used in these studies, our method provided a system-wide assessment of those parameters on endogenous mRNAs.

Despite the high correspondence to in-cell kinetics addressed by single-molecule imaging, our genome-wide data may fuel the ongoing debate. Although a recent single-molecule imaging analysis suggested that translation *per se* may trigger mRNA

destabilization [73], we did not observe a correlation between the translation initiation rate and the mRNA half-life (Figure S5C). The averaged values of the mRNAs in cells may make it challenging to reflect the fate of individual transcripts, as tracked by single-molecule translation/mRNA imaging.

Notably, an earlier study that combined polysome fractionation and RNA-Seq reported a decline in the number of ribosomes longer than 10,000 codons [74]. However, this may stem from the limitation in the dissection of polysomes larger than 8 ribosomes due to the resolution of the sucrose density gradient experiments. In contrast, our method did not have such a limitation and thus detected the correlation between the ribosome numbers and long ORFs (Figure 3D).

Considering cellular contexts that may preferentially allow monoribosomes to drive protein synthesis [75], the stoichiometry of ribosomes on the transcript may be linked to the function of the cell. Ribo-Calibration should help to unveil such a connection between the mode of ribosome stoichiometry and phenotype.

Acknowledgments

We are grateful to all the members of the Iwasaki laboratory for constructive discussions and technical help. We thank Dr. Yukihide Tomari for sharing S2 cells and the rRNA depletion 2′-OMe oligonucleotide pool, and we thank Dr. Yuichiro Mishima for his critical comments. We are grateful to Dr. Yusuke Kimura, Dr. Tomoya Fujita, and Dr. Shiho Makino for sharing the lysates. Computation was supported by the HOKUSAI SailingShip supercomputer facility at RIKEN. This work was supported by the Ministry of Education, Culture, Sports, Science and Technology (MEXT) [a Grant-in-Aid for Transformative Research Areas (B) "Parametric Translation", JP20H05784 (to S.I.), JP20H05786 (to Y.I.), and JP20H05782 (to M.D.); a Grant-in-Aid for Transformative Research Areas (A) "Multifaceted Proteins", JP21H05734, JP23H04268 (to Y.S.)], the Japan Agency for Medical Research and Development (AMED) [AMED-CREST, JP23gm1410001 (to S.I. and Y.I.)], the Japan Society for the Promotion of Science (JSPS) [a Grant-in-Aid for Scientific Research (B), JP23H02415 (to S.I.); a Grant-in-Aid for Early Career Scientists, JP21K15023 (to Y.S.); a Grant-in-Aid for Scientific Research (C), JP23K05648 (to Y.S.)], the Japan Science and Technology Agency (JST) [FOREST Program, JPMJFR226F (to T.M.)], and RIKEN [Pioneering Projects "Biology of Intracellular Environments" (to S.I. and Y.S.]. K.T. was supported by a RIKEN Student Researcher program and a World-leading Innovative Graduate Study Program in Proactive Environmental Studies (WINGS-PES) from The University of Tokyo. Part of the next-generation sequencing was conducted by HiSeq 4000 [supported by the National Institutes for Health (NIH) Instrumentation Grant (S10 OD018174)] in QB3 Genomics, UC Berkeley, Berkeley, CA, (RRID:SCR_022170).

Author contributions

Conceptualization, K.T., M.M., Y.S., and S.I.;

Methodology, K.T., M.M., Y.S., and S.I.;

Formal analysis, K.T., M.M., T.M., S.Y.A.C., and Y.S.;

Investigation, K.T., M.M., T.M., S.Y.A.C., and Y.S.;

Writing – Original Draft, K.T., Y.S., and S.I.;

Writing – Review & Editing, K.T., M.M., T.M., S.Y.A.C., M.D., Y.I., Y.S., and S.I.;

Visualization, K.T.;

Supervision, M.D., Y.I., Y.S., and S.I.;

Funding Acquisition, T.M., M.D., Y.I., Y.S., and S.I.

Declaration of Interests

M.M. and S.I. are inventors on a patent disclosure to RIKEN on technologies described in this manuscript.

Experimental procedures

Cell lines

HEK293 Flp-In T-REx cells (Thermo Fisher Scientific, R78007) and HEK293 cells [American Type Culture Collection (ATCC), CRL-1573] were maintained in DMEM + GlutaMAX-I (Thermo Fisher Scientific) supplemented with 10% fetal bovine serum (FBS, Sigma–Aldrich) at 37°C and 5% CO_2.

For RocA treatment, HEK293 T-REx cells were treated with RocA (Sigma–Aldrich) at a concentration of 0.3 μM or 3 μM and incubated for 30 min before cell lysis. Cells treated with 0.1% DMSO (as a solvent of RocA) were used as controls.

For heat shock treatment, HEK293 cells cultured in 6-well plates were transferred to a water bath set at 43°C and incubated for 0.5, 1, and 2 h. For recovery experiments, cells were returned to 37°C and cultured for 0.5, 1, and 4 h.

Human iPS cells (409B2; RIKEN Bioresource Center Cell Bank, HPS0076) were cultured as previously described [76].

Human neonatal epidermal melanocytes (HEMn-DP, Thermo Fisher Scientific, C2025C) were maintained in Medium 254 (Thermo Fisher Scientific) containing Human Melanocyte Growth Supplement (Thermo Fisher Scientific). Human neonatal dermal fibroblasts (HDFn, Thermo Fisher Scientific, C0045C) were cultured in Medium 106 (Thermo Fisher Scientific) containing LSGS Supplement (Thermo Fisher Scientific). Human neonatal epidermal keratinocytes (HEKn, Thermo Fisher Scientific, C0015C) were cultured in EpiLife Medium (Thermo Fisher Scientific) with HKGS Supplement (Thermo Fisher Scientific). All primary skin cells were maintained at <80% confluency in a 5% CO_2/37°C humidified incubator with the medium changed every other day. The cells were used between passages 3-6.

Fly S2 cells were cultured in Schneider's *Drosophila* medium (Thermo Fisher Scientific) supplemented with 10% inactivated fetal bovine serum (FBS) (Fujifilm Wako Pure Chemical Corporation) and 1% antibiotic-antimycotic solution (Thermo Fisher Scientific) at 28°C.

Mice

Young and aged C57BL/6J male mice were purchased from CREA Japan Inc. Mice were housed under a regular 12-h light/12-h dark cycle (lights on 8:00 and off at 20:00) with free access to food and water. All procedures for mouse experiments were conducted in compliance with the Ethical Regulations of Kyoto University and performed under protocols approved by the Animal Care and Experimentation Committee of Kyoto University.

Plants

Wild-type *Arabidopsis thaliana* (Col-0) seedlings were cultured as previously reported [77].

Bacteria

E. coli MG1655 cells were grown in LB medium at 37°C.

Yeast

Yeast cells (X2180-1a) were cultured in nutrient-rich liquid medium consisting of 1% yeast extract, 2% peptone, and 2% glucose at 30°C.

Preparation of spike-in Rluc-disome and Fluc-trisome

PCR fragments were PCR-amplified using the psiCHECK2-EIF2S3 [32] plasmid as a template with the following forward and reverse primers: Rluc, 5′-TAATACGACTCACTATAGG-3′ and 5′-CACACAAAAAACCAACACACAG-3′; Fluc, 5′-ACTTAATACGACTCACTATAGGAAGCTTGGCATTCCGG-3′ and 5′-TGTATCTTATCATGTCTGCTCGAAG-3′. These DNA fragments were subjected to *in vitro* transcription using a T7-Scribe Standard RNA IVT Kit (CELLSCRIPT). The RNAs were then capped and polyadenylated using a ScriptCap m^7G capping system (CELLSCRIPT), a ScriptCap 2′-*O*-Methyltransferase Kit (CELLSCRIPT), and an A-Plus poly(A) polymerase tailing kit (CELLSCRIPT).

The Rluc mRNA and Fluc mRNA were incubated with rabbit reticulocyte lysate (RRL, Promega) to generate the mRNA-ribosome complex. The reaction mixture consisted of 50 µl of lysate, 30 µl of H_2O, 10 µl of 500 nM mRNA, and 10 µl of premix [100 mM amino acid mixture without methionine (Promega), 100 mM amino acid mixture without leucine (Promega), and 1 U/ml ScriptGuard RNase inhibitor (CELLSCRIPT)]. The mixture was incubated at 30°C for 0.5 h (Rluc mRNA) or 1 h (Fluc mRNA) and mixed with an equal volume of 2× lysis buffer (40 mM Tris-HCl pH 7.5, 300 mM NaCl, 10 mM $MgCl_2$, 2% Triton X-100, 2 mM DTT, 200 µg/ml cycloheximide, and 200 µg/ml chloramphenicol).

The lysates were loaded directly onto a 10-50% sucrose gradient in SDG buffer (20 mM Tris-HCl pH 7.5, 150 mM NaCl, 5 mM $MgCl_2$, 1 mM DTT, 100 µg/ml cycloheximide) and ultracentrifuged at 35,300 rpm and 4°C for 2.5 h using a Himac CP80WX ultracentrifuge (Hitachi) with a P40ST rotor (Hitachi). The gradients were fractionated with continuous measurement of absorbance at 260 nm using a Triax flow cell (BioComp) and micro collector (ATTO). Fractions containing disomes on Rluc

mRNAs or trisomes on Fluc mRNAs were pooled, resulting in a total volume of 1.1 ml for each. These combined fractions were quickly frozen using liquid nitrogen and stored at −80°C.

Ribosome profiling and RNA-Seq

Ribosome profiling libraries were prepared as previously described [12] with some modifications. The libraries prepared in this study are summarized in Table S2.

Lysate preparation

HEK293 T-REx cells were cultured in a 10-cm dish in preparation for RocA treatment, and HEK293 cells were cultured in a well of 6-well plates for heat shock treatment. The cells were then lysed in 500 µl and 100 µl of lysis buffer (20 mM Tris-HCl pH 7.5, 150 mM NaCl, 5 mM $MgCl_2$, 1% Triton X-100, 1 mM DTT, 100 µg/ml cycloheximide, and 100 µg/ml chloramphenicol) and treated with 25 U/ml TURBO DNase (Thermo Fisher Scientific) [12].

Human skin cells cultured in a well of 6-well plates and iPS cells cultured in a well of 12-well plates were lysed in 100 µl of lysis buffer and treated with 25 U/ml TURBO DNase [12].

The mouse forebrain was dissected on ice and disrupted using a loose-fitting Dounce homogenizer in 3 ml ice-cold homogenizing buffer (320 mM sucrose and 5 mM HEPES-KOH pH 7.4). The homogenate was treated with an equal volume of 2× lysis buffer and incubated for 10 min on ice with 25 U/ml TURBO DNase.

S2 cells were seeded in a 10-cm dish, cultured for 3 d, treated with 100 µg/ml cycloheximide, and then collected by immediate centrifugation at 1,000 × *g*. The pellet

was washed with PBS and treated with 400 µl of S2 lysis buffer (20 mM Tris-HCl pH 7.5, 150 mM NaCl, 5 mM $MgCl_2$, 1 mM DTT, 100 µg/ml cycloheximide, 1% Triton X-100, and 25 U/ml TURBO DNase).

E. coli cells grown overnight at 37°C in LB media were diluted 1:100 in fresh LB medium and grown at 37°C until the OD_{600} reached 0.4-0.5 [78]. Cells were then collected by filtration and snap-frozen in liquid nitrogen. The frozen cell pellet and bacterial lysis buffer (20 mM Tris-HCl pH 7.5, 150 mM NH_4Cl, 10 mM $MgCl_2$, 5 mM $CaCl_2$, 1 mM DTT, 100 µg/ml chloramphenicol, and 1% Triton X-100) were disrupted using a Multi-Beads Shocker [Yasui Kikai, MB2200(S)] with a precooled chamber and ball with liquid nitrogen. After thawing at 4°C, the lysate was treated with 25 U/ml TURBO DNase for 10 min on ice.

For yeast, cells were then collected by filtration and snap-frozen in liquid nitrogen with ice grains of lysis buffer and pulverized using a Multi-Beads Shocker with a precooled chamber and ball with liquid nitrogen [79]. The cell lysate was then centrifuged at 3,000 × *g* for 5 min to remove cellular debris. The supernatant was transferred to a new tube and treated with 25 U/ml TURBO DNase.

Two hundred milligrams of snap-frozen *Arabidopsis thaliana* seedlings and ice grains of 400 µl of plant lysis buffer (100 mM Tris-HCl pH 7.5, 40 mM KCl, 20 mM $MgCl_2$, 1 mM DTT, 300 µg/ml chloramphenicol, 100 µg/ml cycloheximide, and 1% Triton X-100) were pulverized using a Multi-Beads Shocker with a precooled chamber and ball with liquid nitrogen [77]. The lysate was clarified by centrifugation at 3,000 × *g* and treated with 25 U/ml TURBO DNase for 10 min on ice.

After DNase treatment, the cell lysate was clarified by centrifugation at 20,000 × *g* for 10 min at 4°C. Total RNA concentrations in the lysates were measured with a Qubit

RNA Broad Range Assay Kit (Thermo Fisher Scientific). Lysates were flash-frozen by liquid nitrogen and stored at −80°C.

Ribo-Calibration

Lysate of HEK293 Flp-In T-REx cells containing 12 µg of total RNA was adjusted to a volume of 338 µl using lysis buffer. Then, 6 µl of Rluc-disome spike-in and 6 µl of Fluc-trisome spike-in were added to the lysate to make a 350 µl lysate solution. For ribosome profiling, 290 µl of the lysate solution (corresponding to 10 µg total RNA) was incubated with 10 µl of 10 U/µl RNase I (Lucigen) for 45 minutes at a temperature of 25°C. For RNA-Seq, the remaining 50 µl of the lysate solution was directly subjected to RNA purification with TRIzol LS reagent (Thermo Fisher Scientific) and a Direct-zol RNA MicroPrep Kit (Zymo Research).

For heat shock experiments that used HEK293 cells, the lysate containing 7 µg total RNA was adjusted to 350 µl.

For human skin cells and iPS cells, the volume of the lysate was adjusted to 350 µl from an initial 100 µl by lysis buffer.

Ribo-FilterOut and rRNA subtraction

After RNase digestion and sucrose cushion ultracentrifugation (at 100,000 rpm for 1 h at 4°C with a TLA110 rotor), the ribosome pellet was resuspended in 150 µl of resuspension buffer (20 mM Tris-HCl pH 7.5, 150 mM NaCl, 5 mM EDTA, 1% Triton X-100, 1 mM DTT, and 20 U/ml SUPERase•In). The mixture was then transferred to the filter cup of an Amicon Ultra 0.5 ml Ultracel 100K centrifugal filter (Millipore) and centrifuged at

14,000 × *g* at 4°C for 10 min. The flow through in the reservoir tube was mixed with TRIzol LS reagent (Thermo Fisher Scientific) and processed for RNA purification.

For EDTA pretreatment, the lysate was treated with 10 mM EDTA for 30 min on ice and then mixed with an additional 10 mM $MgCl_2$ before RNase I digestion. Denaturing UREA-PAGE gel was stained with SYBR Gold (Thermo Fisher Scientific).

For rRNA subtraction, stand-alone Ribo-Zero kits [Ribo-Zero Gold rRNA Removal Kit (Human/Mouse/Rat), Ribo-Zero Gold rRNA Removal Kit (Yeast), Ribo-Zero rRNA Removal Kit (Plant Leaf), and Ribo-Zero rRNA Removal Kit (Bacteria)] or one accompanied by TruSeq Stranded Total RNA Kit (Illumina) was used. For flies, the following biotinylated 2′-*O*-methyl oligonucleotides were used to subtract rRNA fragments on MyOne streptavidin C1 Dynabeads (Thermo Fisher Scientific):
5′-/biotin/AUUGGCAUCACAUCCAUUGUCGUUUA-3′; 5′-/biotin/ACAUCCAUUGUCGUUUAUAAAGUAAA-3′;
5′-/biotin/AUAAACUUUAAAUGGUUUAGAAGCCAU-3′;
5′-/biotin/AAAUGGUUUAGAAGCCAUACAAUGCAAA-3′;
5′-/biotin/GCCUCAUUUAAGAAGGACUUAAAUCGUUAA-3′;
5′-/biotin/AACGCCCCGGGAUUGUGUUAAUUAGCUA-3′;
5′-/biotin/ACGUUAUACGGGCCUGGCACCCUCUAUGGGU-3′;
5′-/biotin/AUUGUUAAUCAUACAAGUGCAUAUAAU-3′;
5′-/biotin/AUAAAUCUAUCAGCACUUUAUCAA-3′; and
5′-/biotin/UUUAAUCAAGUAAGUAAGGAAACA-3′

Harringtonine chase assay

Cells were treated with 2 μg/ml harringtonine (MedChemExpress) at 37°C for 60, 120, and 180 s. Then, cells were treated with 100 μg/ml cycloheximide and incubated for 1 min at 37°C before cell harvest. For no-chase samples, harringtonine treatment was omitted, but cycloheximide was added to the medium.

Library preparation for RNA-Seq

For RNA-Seq library preparation, 0.5 μg of total RNA was used with a TruSeq Stranded mRNA Library Prep Kit (Illumina), or 5 ng of total RNA was used with a SMARTer Stranded Total RNA-Seq Kit v3 (Takara Bio).

Sequencing

Libraries were sequenced on a HiSeq 4000 or HiSeq X system (Illumina) with the pair-end/150 nt-long read option.

Data analysis

Sequence data were processed as previously described [80]. The changes in read count on transcripts were calculated with the DESeq2 package [81] and then renormalized to the mean change of mitochondrial mRNAs (as internal spike-ins) or Rluc and Fluc mRNAs (as external spike-ins) to measure overall alteration.

The absolute ribosome number (N) on transcript j was determined as follows:

$$N_j = (Ribo_j / RNA_j) \times A$$

where $Ribo_j$ represents ribosome footprint reads per million mapped reads (RPM) on the ORF of transcript j, and RNA_j represents transcript per million (TPM) of transcript j. The coefficient A was defined as follows:

$$A = (\sum N_{spike-ins})/[(Ribo_{Rluc}/RNA_{Rluc}) + (Ribo_{Fluc}/RNA_{Fluc})]$$

Theoretically, $Ribo_{Rluc}/RNA_{Rluc}$ and $Ribo_{Fluc}/RNA_{Fluc}$ are 2 and 3, respectively. Thus, the sum of the ribosome number ($\sum N_{spike-ins}$) should be 5. Transcripts with RPM ≥ 1 and TPM ≥ 1 were considered.

The absolute ribosome number (*M)* on each codon *k* of transcript *j* was determined as follows:

$$M_{kj} = (C_k/Ribo_j) \times N_j$$

where C_k represents ribosome footprint RPM on codon *k*.

For the ribosome run-off assay, smoothed metagene profiles were obtained from the transcript possessing the ORF with 2000 codons or longer. The mean read density from 1000 to 1500 codons was set to 1.

The translation initiation rate (*I*) for transcript *j* was defined as follows:

$$N_j = I_j \times D_j$$

where D_j represents the duration of the loaded ribosome on transcript *j*. Given that the loaded ribosome undergoes a translation elongation reaction on the ORF of length L_j in transcript *j*, D_j was defined as follows:

$$D_j = L_j/E$$

where *E* represents the global elongation rate, which was determined to be 4.06 codon/s by ribosome run-off assay. Thus,

$$I_j = E \times N_j/L_j$$

The lifetime translation round (*R*) for transcript *j* was defined as follows:

$$R_j = I_j \times \int_0^{5T_j} \left(\frac{1}{2}\right)^{t/T_j} dt$$

where T_j represents the half-life of transcript j, as determined by BRIC-Seq. Here, we calculated the ribosome loading frequency during $5T_j$, when ~97% of the mRNA is predicted to be degraded.

All the data were provided by the average of replicates when they were available.

Disome footprint data (GSE145723) [19] were processed as described above.

The TOP mRNA definition was performed as described in an earlier study [82].

BRIC-Seq

Library preparation

The libraries prepared in this study are summarized in Table S2. BRIC-Seq was performed as described previously with modifications [52]. HEK293T cells expressing control shRNA [19] were seeded on 10-cm dishes and incubated in 10 ml DMEM with 150 μM bromouridine (BrU, FUJIFILM Wako Pure Chemical Corporation) for 24 h. Cells were then washed twice with 5 ml of DMEM without BrU, incubated in 10 ml of DMEM without BrU for 0, 2, 4, 6, 10, or 24 h, washed with 5 ml PBS, and lysed by adding 600 μl TRIzol reagent (Thermo Fisher Scientific) directly on the dishes. Total RNA was purified using a Direct-zol RNA MiniPrep Plus Kit (Zymo Research).

BrU-containing spike-in mRNAs were synthesized by *in vitro* transcription. Template DNA fragments were PCR-amplified using psiCHECK2 plasmid (Promega) with 5′-TAATACGACTCACTATAGG-3′ and 5′-CACACAAAAAACCAACACACAG-3′ (Rluc); psiCHECK2 plasmid with 5′-ACTTAATACGACTCACTATAGGAAGCTTGGCATTCCGG-3′ and 5′-TGTATCTTATCATGTCTGCTCGAAG-3′ (Fluc); pColdI-GFP plasmid [83] with 5′-TGACTAATACGACTCACTATAGGATCTGTAAAGCACGCCATATCG-3′ and 5′-

TGGCAGGGATCTTAGATTCTG-3′ (GFP). *In vitro* transcription was performed using a T7-Scribe Standard RNA IVT Kit (CELLSCRIPT) in the presence of 1.2 mM BrUTP (Jena Bioscience) and 5 mM UTP. RNA was purified by RNAClean XP beads (Beckman Coulter).

For immunoprecipitation, 25 µl of Dynabeads M-280 Sheep anti-Mouse IgG (Thermo Fisher Scientific) was incubated with 2 mg of anti-BrdU antibody (BD Bioscience, 555627) for 3 h at 4°C and equilibrated with BRIC-Seq lysis buffer (lysis buffer without cycloheximide and chloramphenicol). Twenty micrograms of total RNA mixed with spike-in RNA mixture (1 ng Rluc, 0.2 ng Fluc, and 0.04 ng GFP) was incubated with the magnetic beads in BRIC-Seq lysis buffer for 2 h at 4°C, washed with 100 µl of BRIC-Seq lysis buffer five times, and mixed with 200 µl of TRIzol reagent. RNA was extracted by a Direct-zol RNA MicroPrep Kit and subjected to RNA-Seq library preparation using a Ribo-Zero Gold rRNA Removal Kit (Human/Mouse/Rat) (Illumina) followed by a TruSeq Stranded Total RNA Kit (Illumina).

Sequencing

Libraries were sequenced on a HiSeq 4000 (Illumina) with the single-end/50 nt-long read option.

Data analysis

Filtering, trimming adapters, and mapping to the genome were performed as described in the RNA-Seq section. The fold-changes of read counts compared to 0 h samples were calculated with the DESeq2 package [81] and then renormalized to the mean change of three spike-ins. For the calculation of mRNA half-life, the $\log_2$-converted fold-change of each

time point was fitted to a linear model. Since the decay of transcripts sometimes slows at later time points, we calculated the half-life using all combinations of earlier samples (*i.e.*, 0-4 h, 0-6 h, 0-10 h, and 0-24 h) and adopted a fitting with the maximum R^2 value. Transcripts with $R^2 > 0.9$ and $0 <$ half-life < 24 h were used in downstream analysis.

Nascent peptide labeling by OP-puro

Cells seeded in 6-well plates were treated with 20 μM OP-puro (Jena Bioscience) at 37°C for 30 min, washed with 1 ml of phosphate-buffered saline (PBS), and lysed in 100 μl of OP-puro lysis buffer (20 mM Tris-HCl pH 7.5, 150 mM NaCl, 5 mM $MgCl_2$, and 1% Triton X-100). The lysate was then incubated with 1 μM IRDye 800CW azide (LI-COR Bioscience) for 30 min at 25°C using a Click-iT Cell Reaction Buffer Kit (Thermo Fisher Scientific). After the removal of unreacted azide by MicroSpin G-25 columns (Cytiva), proteins were separated by sodium dodecyl sulfate (SDS)-polyacrylamide gel electrophoresis (PAGE). The infrared (IR) 800 signal was then detected using ODYSSEY CLx (LI-COR Biosciences). The total protein on the gel was stained with EzStain AQua (ATTO) and detected by ODYSSEY CLx (LI-COR Biosciences) with an IR700 channel. Total protein-normalized nascent peptide signals were quantified after subtraction of the background.

Western blotting

The following primary antibodies were used: anti-HSP70 (Cell Signaling Technology, #4872; 1:1000) and anti-β-actin (LI-COR Biosciences, #926-42212; 1:1000). For secondary antibodies, we utilized IRDye 800CW anti-rabbit IgG (LI-COR Biosciences, #926-32211: 1:10000) and IRDye 680RD anti-mouse IgG (LI-COR Biosciences, #925-

68070: 1:10000). The images were subsequently captured using the ODYSSEY CLx system (LI-COR Biosciences).

Cell viability assay

Cells were seeded in white 96-well plates and incubated with the RealTime-Glo MT Cell Viability Assay (Promega). Luminescence was detected using a GloMax-96 instrument (Promega).

Accession numbers

The ribosome profiling and RNA-Seq data obtained in this study (GSE233555) were deposited in the National Center for Biotechnology Information (NCBI) database. This study also used deposited disome profiling data (GSE145723) [19] and BRIC-Seq data (GSE233374).

Figure and table legends

Figure 1. Biochemical separation of ribosome footprints from ribosome subunits reduces contamination by rRNA fragments in ribosome profiling.

(A) Schematic of rRNA depletion methods. The hybridization of biotinylated oligonucleotides and subsequent subtraction on streptavidin beads has been a common strategy ("standard method"). In contrast, Ribo-FilterOut is based on the separation of ribosome footprints from large and small ribosome subunits by ultrafiltration.

(B) Reads obtained in ribosome profiling were mapped to the indicated RNAs and then genome sequence. The mean (bar) and individual replicates (n = 2, point) are shown. RPM, reads per million mapped reads.

(C) Pearson's correlation coefficients (*r*) for reads on each transcript. The indicated experimental conditions were compared. The color scales for *r* are shown.

See also Figures S1 and S2 and Table S2.

Figure 2. Purified mRNA-ribosome complexes serve as spike-in controls to measure the global change in translation.

(A) Schematic of ribosome profiling experiments supplemented with di-ribosome and tri-ribosome-assembled mRNAs as spike-ins.

(B and C) Histograms of ribosome footprint fold change with 0.3 or 3 μM RocA treatment with (C) or without (B) normalization by Ribo-Calibration spike-ins.

(D and E) Histograms of RNA fold change with 0.3 or 3 μM RocA treatment with (E) or without (D) normalization by Ribo-Calibration spike-ins.

See also Figure S3 and Table S2.

Figure 3. The absolute calibration of ribosome numbers on transcripts.

(A) Schematic of the absolute ribosome number calculation by ribosome profiling and RNA-Seq with Ribo-Calibration.

(B) Comparison of expected and observed ribosome numbers on Rluc and Fluc transcripts used for Ribo-Calibration.

(C) Histogram of the absolute ribosome number on transcripts.

(D) Box plots of the absolute number of ribosomes along ORF length.

(E) Histogram of the distance between ribosomes, with the zoomed-in inset highlighting tightly packed transcripts.

(F) GO terms enriched in the tightly packed transcripts, defined in E. The color scales for significance and the size scales for gene number in each category are shown.

(G) Metagene plots with calibrated ribosome numbers at each position around start codons (left, the first position of the start codon was set to 0) and stop codons (right, the first position of the stop codon was set to 0).

See also Figure S4, Tables S1, and S2.

Figure 4. The kinetic parameters revealed by Ribo-Calibration.

(A) The smoothed metagene plots with ribosome run-off assay with harringtonine (HAR) chase.

(B) The expansion of the ribosome-free area over time by harringtonine chase. The linear regression determines the global elongation rates as 4.1 codon/s.

(C) Histogram of the translation initiation rate across transcripts.

(D) Box plots of the translation initiation rate for TOP and non-TOP transcripts.

(E) The histogram of the transcript half-lives, determined by BRIC-Seq.

(F) Histogram of the lifetime translation rounds before transcript decay.

(G) Schematic summary of kinetic numbers regarding translation identified in this study.

See also Figure S5, Tables S1, and S2.

Figure 5. Ribosome flux on transcripts during heat shock stress and the recovery states.

(A and B) Box plots of ribosome footprint fold change (A) and RNA fold change (B) during heat shock and recovery with normalization by Ribo-Calibration spike-ins.

(C) Box plots of the absolute ribosome number on transcripts during heat shock and recovery.

(D and E) Box plots of ribosome footprint fold change (D) and RNA fold change (E) for *Hsp70* family genes during heat shock and recovery with normalization by Ribo-Calibration spike-ins.

(F) Box plots of the absolute ribosome number on transcripts of *Hsp70* family genes during heat shock and recovery.

(G and H) Dot plots of the absolute ribosome number on transcripts for the indicated genes during heat shock and recovery.

See also Figure S6 and Table S2.

Figure 6. Transcriptome-wide ribosome flux in cell types and aged tissues.

(A) Box plots of the absolute ribosome number on transcripts in the indicated materials.

(B) Dot plots of the absolute ribosome number on transcripts for the indicated genes in melanocytes, fibroblasts, and keratinocytes.

(C) Relative OP-puro incorporation in HEK293 T-REx cells and HEK293 cells.

(D) Relative cell growth rate of HEK293 T-REx cells and HEK293 cells. The mean (point) and s.d. (error) from three replicates are shown.

(E and F) Histograms of ribosome footprint fold change (E) and RNA fold change (F) in young or aged mouse forebrains with normalization by Ribo-Calibration spike-ins.

(G) Heatmap of the distance between ribosomes in young and aged mouse forebrains. The color scales for the Z score are shown. See Figure S8E for the cluster definition.

See also Figures S7 and S8 and Table S2.

Figure S1. Characterization of the Ribo-FilterOut technique, related to Figure 1.

(A) Schematic of the experiments in (B). Right: mRNA-ribosome complexes were treated with RNase I, and then the ribosomal complex was isolated by ultracentrifugation. Ribosome footprints were separated from ribosome subunits by EDTA treatment and then isolated by ultrafiltration. Left: for the control, the lysate was pretreated with EDTA to release mRNA from ribosomes before RNase I digestion.

(B) SYBR Gold staining of the RNA fragments obtained by the experiments shown in (A).

(C) The distribution of ribosome footprint length in ribosome profiling for the indicated conditions.

(D) Metagene plots of the 5′ end of ribosome footprints around the start codon (the first position of the start codon was set on 0) along the footprint length. The color scales for read abundance are shown. RPM, reads per million mapped reads.

Figure S2. Application of Ribo-FilterOut to various species, related to Figure 1.

(A-D) The combination of the conventional rRNA subtraction method [pullout with 2′-*O*-methyl (2′-Ome)-modified oligonucleotide hybridization or Ribo-Zero] with Ribo-FilterOut for fly S2 cells (A), yeast (B), plants (C), and bacteria (D). RPM, reads per million mapped reads.

Figure S3. Characterization of the method for global translation measurement by Ribo-Calibration, related to Figure 2.

(A) Sucrose density gradient ultracentrifugation for the separation of ribosomal complexes. Rluc mRNA (left) and Fluc mRNA (right) were translated *in vitro* with RRL. Highlighted fractions were isolated for the spike-ins for ribosome profiling.

(B) Ribosome footprint coverage on RLuc mRNA (left) and Fluc mRNA (right). RPM, reads per million mapped reads.

(C) Fraction of the frame position where the 5′ ends of reads are located. Twenty-nine-nucleotide-long footprints were analyzed. The mean (bar) and individual data (n = 6; 2 replicates for DMSO, 2 replicates for 0.3 μM RocA treatment, and 2 replicates for 3 μM RocA treatment) are shown.

(D) Histograms of ribosome footprint fold change with 0.3 or 3 μM RocA treatment with normalization by mitochondrial footprints.

Figure S4. Characterization of the method for the absolute calibration of ribosome number by Ribo-Calibration, related to Figure 3.

(A) Histograms of the absolute ribosome number on transcripts with 0.3 or 3 μM RocA treatment.

(B) Histograms of the distance between ribosomes with 0.3 or 3 μM RocA treatment.

(C) MA (M, log ratio; A, mean average) plot of the ribosome footprint fold change with 3 μM RocA treatment with normalization by Ribo-Calibration spike-ins. Transcripts with significant changes (FDR < 0.05) are highlighted.

(D) Box plots of the absolute number of ribosomes for RocA high-sensitivity transcripts (left) and low-sensitivity transcripts (right).

(E) Scatter plots of the distance between ribosomes and disome occupancy. RPM, reads per million mapped reads.

(F and G) Distribution of ribosome footprints along the indicated genes. The A-site position of reads is depicted. The calibrated ribosome numbers on the pause site in *XBP1u* and uORF0 in *ATF4* (including ribosomes on codons before and ahead) are highlighted.

Figure S5. Characterization of ribosome run-off assay and BRIC-Seq, related to Figure 4.

(A) Schematic of the ribosome run-off assay with harringtonine (HAR) chase. After a short incubation with HAR, ribosomes on the transcripts were fixed by cycloheximide (CHX).

(B) Schematic of BRIC-Seq with bromo uridine (BrU). After labeling cellular mRNA with BrU, cells were incubated in medium without BrU along the time course. mRNAs were isolated with the anti-BrdU antibody.

(C) Comparison of transcript half-life and the absolute number of ribosomes on transcripts (left), the distance between ribosomes (middle), and the translation initiation rate (right). *r*, Pearson's correlation coefficient.

Figure S6. Characterization of heat shock and recovery in HEK293 cells, related to Figure 5.

(A) Schematic of the experiments along the time course.

(B) Relative OP-puro incorporation during heat shock and recovery. The mean (bar), s.d. (error), and individual data (n = 3, point) are shown.

(C) Western blotting of the indicated proteins.

(D) Comparison of expected and observed ribosome numbers on Rluc and Fluc transcripts used for Ribo-Calibration.

(E) Box plots of the distance between ribosomes during heat shock and recovery.

(F) Metagene plots with relative ribosome occupancy at each position around start codons (left, the first position of the start codon was set to 0) and stop codons (right, the first position of the stop codon was set to 0) under the indicated conditions.

(G) Metagene plots with calibrated ribosome numbers at each position around start codons (left, the first position of the start codon was set to 0) and stop codons (right, the first position of the stop codon was set to 0) under the indicated conditions.

Figure S7. Characterization of ribosome profiling with Ribo-Calibration in skin cells, related to Figure 6.

(A) The morphology of the indicated skin cells. Scale bar, 100 μm.

(B) Comparison of expected and observed ribosome numbers on Rluc and Fluc transcripts used for Ribo-Calibration.

(C) Histograms of the absolute ribosome number on transcripts in the indicated skin cells.

(D) Histograms of the distance between ribosomes in the indicated skin cells.

(E) Metagene plots with calibrated ribosome numbers at each position around start codons (left, the first position of the start codon was set to 0) and stop codons (right, the first position of the stop codon was set to 0) in the indicated skin cells.

(F-G) Heatmap of the distance between ribosomes in the indicated skin cells. The color scales for the Z score are shown.

(H-L) GO terms enriched in the gene clusters, defined in F. The color scales for significance and the size scales for gene number in each category are shown.

Figure S8. Characterization of ribosome profiling with Ribo-Calibration in mouse forebrains, related to Figure 6.

(A) Comparison of expected and observed ribosome numbers on Rluc and Fluc transcripts used for Ribo-Calibration.

(B) Histograms of the absolute ribosome number on transcripts in the young and aged mouse forebrains.

(C) Histograms of the distance between ribosomes in the young and aged mouse forebrains.

(D) The metagene plots with calibrated ribosome number on each position around start codons (left, the first position of the start codon was set to 0) and stop codons (right, the first position of the stop codon was set to 0) in the young and aged mouse forebrains.

(E) Heatmap of the distance between ribosomes in young and aged mouse forebrains. The color scales for the Z score are shown.

(F-G) GO terms enriched in the gene clusters, defined in E. The color scales for significance and the size scales for gene number in each category are shown.

Table S1. List of stoichiometric and kinetic parameters obtained in this study, related to Figures 3 and 4.

Each transcript is listed with its Ensembl transcript ID, ORF length (nt), absolute ribosome number on the ORF, distance between ribosomes (nt), translation initiation (s/event), half-life (h), and translation round before transcript decay (event).

Table S2. List of deep sequencing data used in this study, related to Figures 1-6.

Each data set is listed with library name, treatment, species name, cell line or strain name, rRNA depletion method, Ribo-Calibration application, replicate number, data type, RNA-Seq kit name, input amount, reference, and accession number.

References

1. Ingolia, N. T., Ghaemmaghami, S., Newman, J. R. & Weissman, J. S. Genome-wide analysis *in vivo* of translation with nucleotide resolution using ribosome profiling. *Science* **324**, 218–223 (2009).
2. Brar, G. A. & Weissman, J. S. Ribosome profiling reveals the what, when, where and how of protein synthesis. *Nat. Rev. Mol. Cell Biol.* **16**, 651–664 (2015).
3. Iwasaki, S. & Ingolia, N. T. The growing toolbox for protein synthesis studies. *Trends Biochem. Sci.* **42**, 612–624 (2017).
4. Ingolia, N. T., Hussmann, J. A. & Weissman, J. S. Ribosome profiling: Global views of translation. *Cold Spring Harb. Perspect. Biol.* **11**, (2019).
5. Wang, Y., Zhang, H. & Lu, J. Recent advances in ribosome profiling for deciphering translational regulation. *Methods* **176**, 46–54 (2020).
6. Steitz, J. A. Polypeptide chain initiation: nucleotide sequences of the three ribosomal binding sites in bacteriophage R17 RNA. *Nature* **224**, 957–964 (1969).
7. Kozak, M. & Shatkin, A. J. Characterization of ribosome-protected fragments from reovirus messenger RNA. *J. Biol. Chem.* **251**, 4259–4266 (1976).
8. Wolin, S. L. & Walter, P. Ribosome pausing and stacking during translation of a eukaryotic mRNA. *EMBO J.* **7**, 3559–3569 (1988).
9. Ingolia, N. T., Brar, G. A., Rouskin, S., McGeachy, A. M. & Weissman, J. S. The ribosome profiling strategy for monitoring translation *in vivo* by deep sequencing of ribosome-protected mRNA fragments. *Nat. Protoc.* **7**, 1534–1550 (2012).
10. Weinberg, D. E. *et al.* Improved ribosome-footprint and mRNA measurements provide insights into dynamics and regulation of yeast translation. *Cell Rep.* **14**,

1787–1799 (2016).

11. McGlincy, N. J. & Ingolia, N. T. Transcriptome-wide measurement of translation by ribosome profiling. *Methods* **126**, 112–129 (2017).
12. Mito, M., Mishima, Y. & Iwasaki, S. Protocol for disome profiling to survey ribosome collision in humans and zebrafish. *STAR Protoc* **1**, 100168 (2020).
13. Zinshteyn, B., Wangen, J. R., Hua, B. & Green, R. Nuclease-mediated depletion biases in ribosome footprint profiling libraries. *RNA* **26**, 1481–1488 (2020).
14. Alkan, F., Silva, J., Pintó Barberà, E. & Faller, W. J. Ribo-ODDR: oligo design pipeline for experiment-specific rRNA depletion in Ribo-seq. *Bioinformatics* **37**, 2659–2667 (2021).
15. Choe, D. *et al.* RiboRid: A low cost, advanced, and ultra-efficient method to remove ribosomal RNA for bacterial transcriptomics. *PLoS Genet.* **17**, e1009821 (2021).
16. Gu, H., Sun, Y. H. & Li, X. Z. Novel rRNA-depletion methods for total RNA sequencing and ribosome profiling developed for avian species. *Poult. Sci.* **100**, 101321 (2021).
17. Chung, B. Y. *et al.* The use of duplex-specific nuclease in ribosome profiling and a user-friendly software package for Ribo-seq data analysis. *RNA* **21**, 1731–1745 (2015).
18. Gu, W. *et al.* Depletion of Abundant Sequences by Hybridization (DASH): using Cas9 to remove unwanted high-abundance species in sequencing libraries and molecular counting applications. *Genome Biol.* **17**, 41 (2016).
19. Han, P. *et al.* Genome-wide survey of ribosome collision. *Cell Rep.* **31**, 107610 (2020).

20. Wilkins, O. G. & Ule, J. Ribocutter: Cas9-mediated rRNA depletion from multiplexed Ribo-seq libraries. *bioRxiv* (2021) doi:10.1101/2021.07.14.451473.

21. Jiang, L. *et al.* Synthetic spike-in standards for RNA-seq experiments. *Genome Res.* **21**, 1543–1551 (2011).

22. Lovén, J. *et al.* Revisiting global gene expression analysis. *Cell* **151**, 476–482 (2012).

23. Chen, K. *et al.* The overlooked fact: fundamental need for spike-in control for virtually all genome-wide analyses. *Mol. Cell. Biol.* **36**, 662–667 (2015).

24. Han, Y. *et al.* Monitoring cotranslational protein folding in mammalian cells at codon resolution. *Proc. Natl. Acad. Sci. U. S. A.* **109**, 12467–12472 (2012).

25. Andreev, D. E. *et al.* Translation of 5' leaders is pervasive in genes resistant to eIF2 repression. *Elife* **4**, e03971 (2015).

26. Popa, A., Lebrigand, K., Barbry, P. & Waldmann, R. Pateamine A-sensitive ribosome profiling reveals the scope of translation in mouse embryonic stem cells. *BMC Genomics* **17**, 52 (2016).

27. Arpat, A. B. *et al.* Transcriptome-wide sites of collided ribosomes reveal principles of translational pausing. *Genome Res.* **30**, 985–999 (2020).

28. Wang, Y. J. *et al.* Lso2 is a conserved ribosome-bound protein required for translational recovery in yeast. *PLoS Biol.* **16**, e2005903 (2018).

29. Haneke, K. *et al.* CDK1 couples proliferation with protein synthesis. *J. Cell Biol.* **219**, (2020).

30. Wang, Y. J. & Gilbert, W. V. Quantitative Comparisons of Translation Activity by Ribosome Profiling with Internal Standards. in *Ribosome Profiling: Methods and Protocols* (ed. Labunskyy, V. M.) 127–149 (Springer US, 2021).

31. Hoerth, K., Reitter, S. & Schott, J. Normalized Ribo-Seq for Quantifying Absolute Global and Specific Changes in Translation. *Bio Protoc* **12**, e4323 (2022).
32. Iwasaki, S., Floor, S. N. & Ingolia, N. T. Rocaglates convert DEAD-box protein eIF4A into a sequence-selective translational repressor. *Nature* **534**, 558–561 (2016).
33. Liu, T. Y. *et al.* Time-Resolved Proteomics Extends Ribosome Profiling-Based Measurements of Protein Synthesis Dynamics. *Cell Syst* **4**, 636–644.e9 (2017).
34. Iwasaki, S. *et al.* The translation inhibitor rocaglamide targets a bimolecular cavity between eIF4A and polypurine RNA. *Mol. Cell* **73**, 738–748.e9 (2019).
35. Chen, M. *et al.* Dual targeting of DDX3 and eIF4A by the translation inhibitor rocaglamide A. *Cell Chem Biol* **28**, 475–486.e8 (2021).
36. Chhipi-Shrestha, J. K. *et al.* Splicing modulators elicit global translational repression by condensate-prone proteins translated from introns. *Cell Chemical Biology* vol. 29 259–275.e10 Preprint at https://doi.org/10.1016/j.chembiol.2021.07.015 (2022).
37. Lareau, L. F., Hite, D. H., Hogan, G. J. & Brown, P. O. Distinct stages of the translation elongation cycle revealed by sequencing ribosome-protected mRNA fragments. *Elife* **3**, e01257 (2014).
38. Wu, C. C., Zinshteyn, B., Wehner, K. A. & Green, R. High-resolution ribosome profiling defines discrete ribosome elongation states and translational regulation during cellular stress. *Mol. Cell* **73**, 959–970.e5 (2019).
39. Chu, J. *et al.* CRISPR-mediated drug-target validation reveals selective pharmacological inhibition of the RNA helicase, eIF4A. *Cell Rep.* **15**, 2340–2347 (2016).

40. Chu, J. *et al.* Rocaglates induce gain-of-function alterations to eIF4A and eIF4F. *Cell Rep.* **30**, 2481–2488.e5 (2020).

41. Shichino, Y. & Iwasaki, S. Compounds for selective translational inhibition. *Curr. Opin. Chem. Biol.* **69**, 102158 (2022).

42. Meydan, S. & Guydosh, N. R. Disome and trisome profiling reveal genome-wide targets of ribosome quality control. *Mol. Cell* **79**, 588–602.e6 (2020).

43. Zhao, T. *et al.* Disome-seq reveals widespread ribosome collisions that promote cotranslational protein folding. *Genome Biol.* **22**, 16 (2021).

44. Meydan, S. & Guydosh, N. R. A cellular handbook for collided ribosomes: surveillance pathways and collision types. *Curr. Genet.* **67**, 19–26 (2021).

45. Kim, K. Q. & Zaher, H. S. Canary in a coal mine: collided ribosomes as sensors of cellular conditions. *Trends Biochem. Sci.* **47**, 82–97 (2022).

46. Yanagitani, K., Kimata, Y., Kadokura, H. & Kohno, K. Translational pausing ensures membrane targeting and cytoplasmic splicing of XBP1u mRNA. *Science* **331**, 586–589 (2011).

47. Ingolia, N. T., Lareau, L. F. & Weissman, J. S. Ribosome profiling of mouse embryonic stem cells reveals the complexity and dynamics of mammalian proteomes. *Cell* **147**, 789–802 (2011).

48. Shanmuganathan, V. *et al.* Structural and mutational analysis of the ribosome-arresting human XBP1u. *Elife* **8**, e46267 (2019).

49. Wagner, S. *et al.* Selective translation complex profiling reveals staged initiation and co-translational assembly of initiation factor complexes. *Mol. Cell* **79**, 546–560.e7 (2020).

50. Gerashchenko, M. V., Peterfi, Z., Yim, S. H. & Gladyshev, V. N. Translation

elongation rate varies among organs and decreases with age. *Nucleic Acids Res.* **49**, e9 (2021).

51. Meyuhas, O. & Kahan, T. The race to decipher the top secrets of TOP mRNAs. *Biochim. Biophys. Acta* **1849**, 801–811 (2015).
52. Tani, H. *et al.* Genome-wide determination of RNA stability reveals hundreds of short-lived noncoding transcripts in mammals. *Genome Res.* **22**, 947–956 (2012).
53. Paulsen, M. T. *et al.* Coordinated regulation of synthesis and stability of RNA during the acute TNF-induced proinflammatory response. *Proc. Natl. Acad. Sci. U. S. A.* **110**, 2240–2245 (2013).
54. Shalgi, R. *et al.* Widespread regulation of translation by elongation pausing in heat shock. *Mol. Cell* **49**, 439–452 (2013).
55. Alagar Boopathy, L. R., Jacob-Tomas, S., Alecki, C. & Vera, M. Mechanisms tailoring the expression of heat shock proteins to proteostasis challenges. *J. Biol. Chem.* **298**, 101796 (2022).
56. Pakos-Zebrucka, K. *et al.* The integrated stress response. *EMBO Rep.* **17**, 1374–1395 (2016).
57. Wek, R. C. Role of eIF2α kinases in translational control and adaptation to cellular stress. *Cold Spring Harb. Perspect. Biol.* **10**, a032870 (2018).
58. Liu, B., Han, Y. & Qian, S. B. Cotranslational response to proteotoxic stress by elongation pausing of ribosomes. *Mol. Cell* **49**, 453–463 (2013).
59. Lee, J.-S. *et al.* Comparison of gene expression profiles between keratinocytes, melanocytes and fibroblasts. *Ann. Dermatol.* **25**, 36–45 (2013).
60. Reemann, P. *et al.* Melanocytes in the skin – comparative whole transcriptome analysis of main skin cell types. *PLoS One* **9**, e115717 (2014).

61. Raposo, G. & Marks, M. S. Melanosomes—dark organelles enlighten endosomal membrane transport. *Nat. Rev. Mol. Cell Biol.* **8**, 786–797 (2007).

62. Pilling, D., Vakil, V., Cox, N. & Gomer, R. H. TNF-α-stimulated fibroblasts secrete lumican to promote fibrocyte differentiation. *Proc. Natl. Acad. Sci. U. S. A.* **112**, 11929–11934 (2015).

63. Woodward, K. & Shirokikh, N. E. Translational control in cell ageing: an update. *Biochem. Soc. Trans.* **49**, 2853–2869 (2021).

64. Anisimova, A. S. *et al.* Multifaceted deregulation of gene expression and protein synthesis with age. *Proc. Natl. Acad. Sci. U. S. A.* **117**, 15581–15590 (2020).

65. Kim, H. S. & Pickering, A. M. Protein translation paradox: Implications in translational regulation of aging. *Front Cell Dev Biol* **11**, 1129281 (2023).

66. Tatavarty, V. *et al.* Single-molecule imaging of translational output from individual RNA granules in neurons. *Mol. Biol. Cell* **23**, 918–929 (2012).

67. Morisaki, T. *et al.* Real-time quantification of single RNA translation dynamics in living cells. *Science* **352**, 1425–1429 (2016).

68. Wu, B., Eliscovich, C., Yoon, Y. J. & Singer, R. H. Translation dynamics of single mRNAs in live cells and neurons. *Science* **352**, 1430–1435 (2016).

69. Yan, X., Hoek, T. A., Vale, R. D. & Tanenbaum, M. E. Dynamics of translation of single mRNA molecules *in vivo*. *Cell* **165**, 976–989 (2016).

70. Wang, C., Han, B., Zhou, R. & Zhuang, X. Real-time imaging of translation on single mRNA transcripts in live cells. *Cell* **165**, 990–1001 (2016).

71. Voigt, F. *et al.* Single-molecule quantification of translation-dependent association of mRNAs with the endoplasmic reticulum. *Cell Rep.* **21**, 3740–3753 (2017).

72. Livingston, N. M. *et al.* Bursting translation on single mRNAs in live cells. *Mol.*

Cell (2023) doi:10.1016/j.molcel.2023.05.019.

73. Dave, P. *et al.* Single-molecule imaging reveals translation-dependent destabilization of mRNAs. *Mol. Cell* **83**, 589–606.e6 (2023).
74. Sugimoto, Y. & Ratcliffe, P. J. Isoform-resolved mRNA profiling of ribosome load defines interplay of HIF and mTOR dysregulation in kidney cancer. *Nat. Struct. Mol. Biol.* **29**, 871–880 (2022).
75. Bourke, A. M., Schwarz, A. & Schuman, E. M. De-centralizing the central dogma: mRNA translation in space and time. *Mol. Cell* **83**, 452–468 (2023).
76. Chow, S. Y. A. *et al.* Human sensory neurons modulate melanocytes through secretion of RGMB. *Cell Rep.* **40**, 111366 (2022).
77. Kurihara, Y. *et al.* Transcripts from downstream alternative transcription start sites evade uORF-mediated inhibition of gene expression in *Arabidopsis*. *Proc. Natl. Acad. Sci. U. S. A.* **115**, 7831–7836 (2018).
78. Fujita, T. *et al.* The landscape of translational stall sites in bacteria revealed by monosome and disome profiling. *RNA* **28**, 290–302 (2022).
79. Makino, S., Kawamata, T., Iwasaki, S. & Ohsumi, Y. Selectivity of mRNA degradation by autophagy in yeast. *Nat. Commun.* **12**, 2316 (2021).
80. Kashiwagi, K. *et al.* eIF2B-capturing viral protein NSs suppresses the integrated stress response. *Nat. Commun.* **12**, 1–12 (2021).
81. Love, M. I., Huber, W. & Anders, S. Moderated estimation of fold change and dispersion for RNA-seq data with DESeq2. *Genome Biol.* **15**, 550 (2014).
82. Philippe, L., van den Elzen, A. M. G., Watson, M. J. & Thoreen, C. C. Global analysis of LARP1 translation targets reveals tunable and dynamic features of 5′ TOP motifs. *Proc. Natl. Acad. Sci. U. S. A.* **117**, 5319–5328 (2020).

83. Tsuboyama, K. *et al.* A widespread family of heat-resistant obscure (Hero) proteins protect against protein instability and aggregation. *PLoS Biol.* **18**, e3000632 (2020).

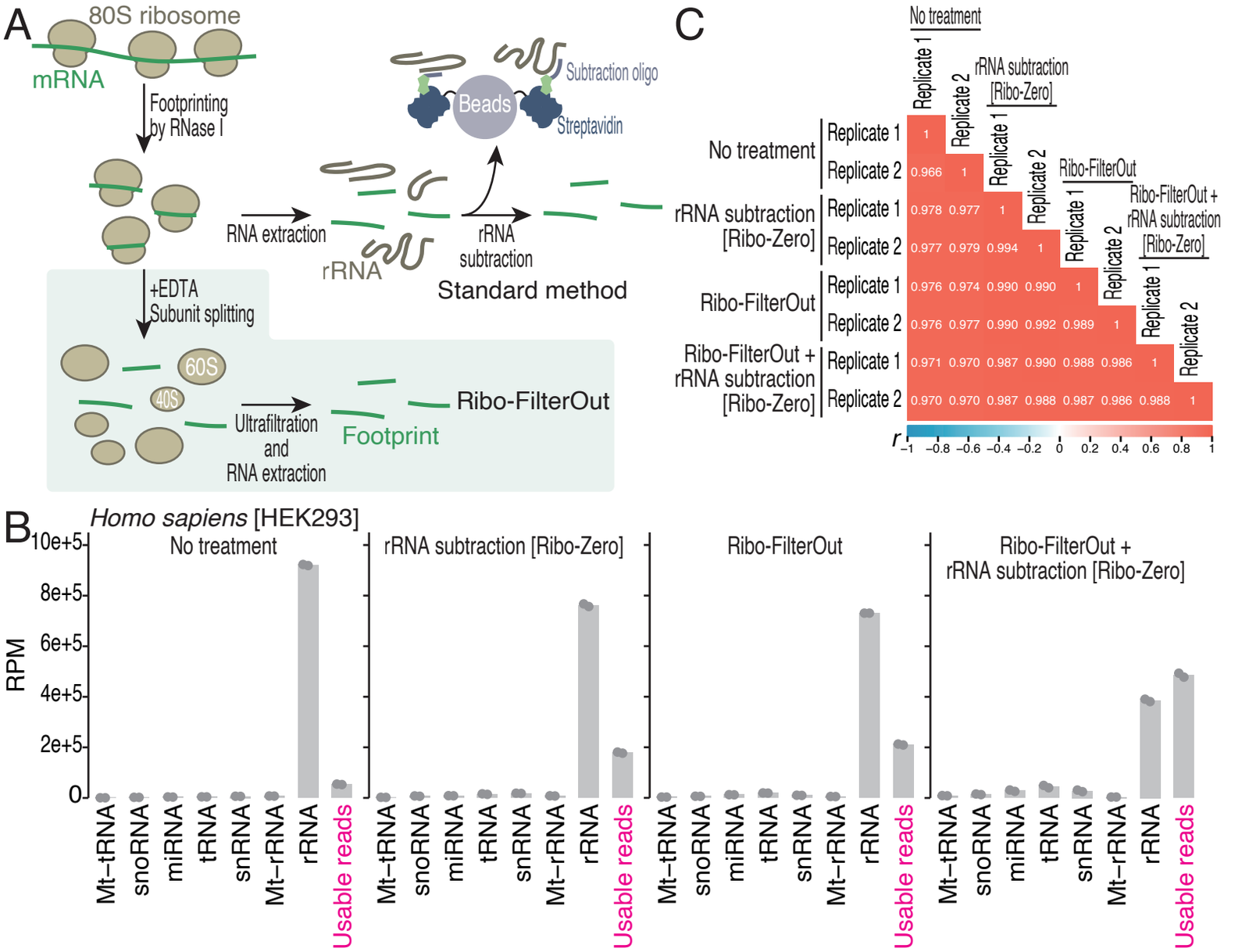

Figure 1 Tomuro, Mito *et al.* (2023)

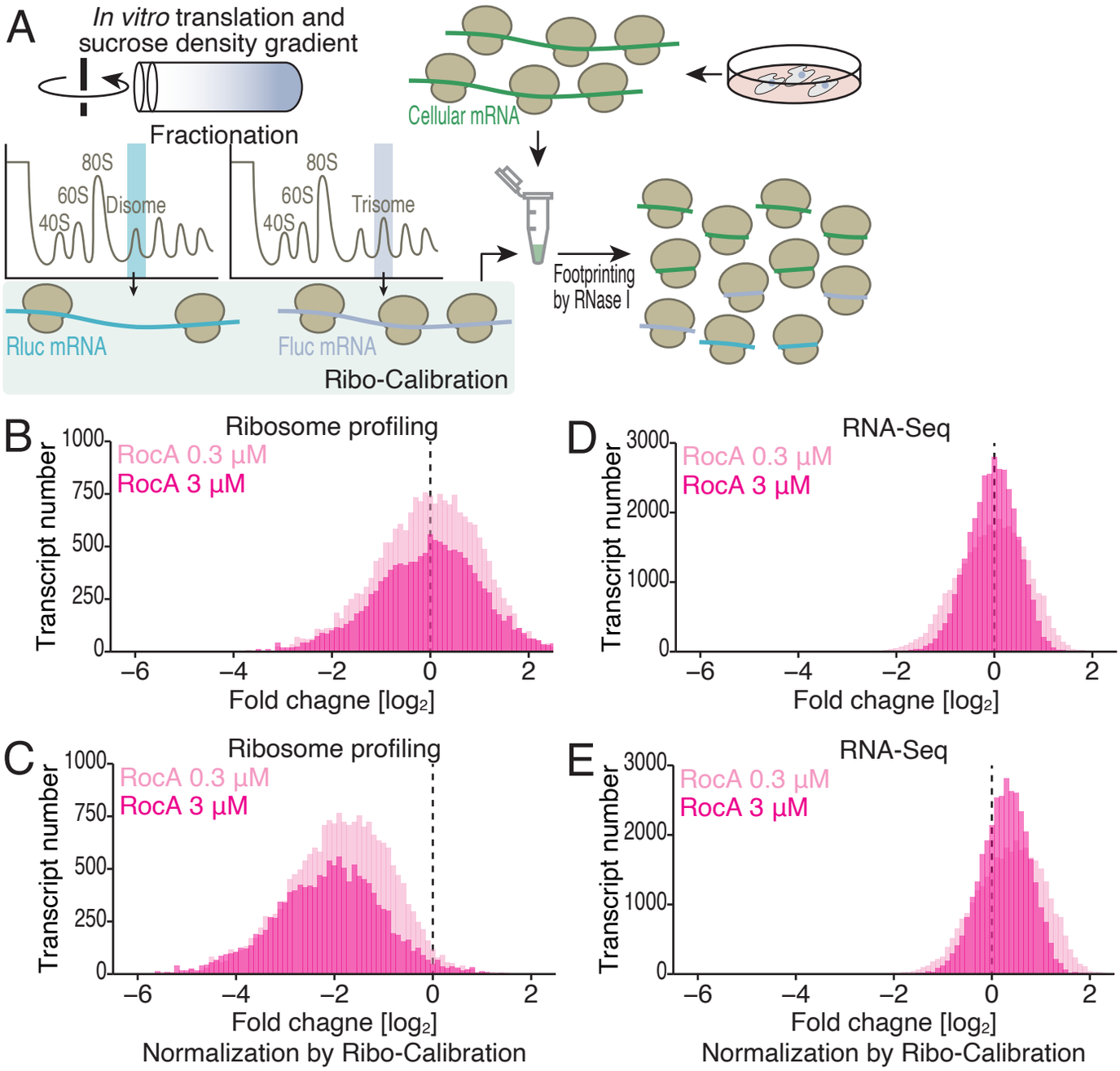

Figure 2 Tomuro, Mito *et al.* (2023)

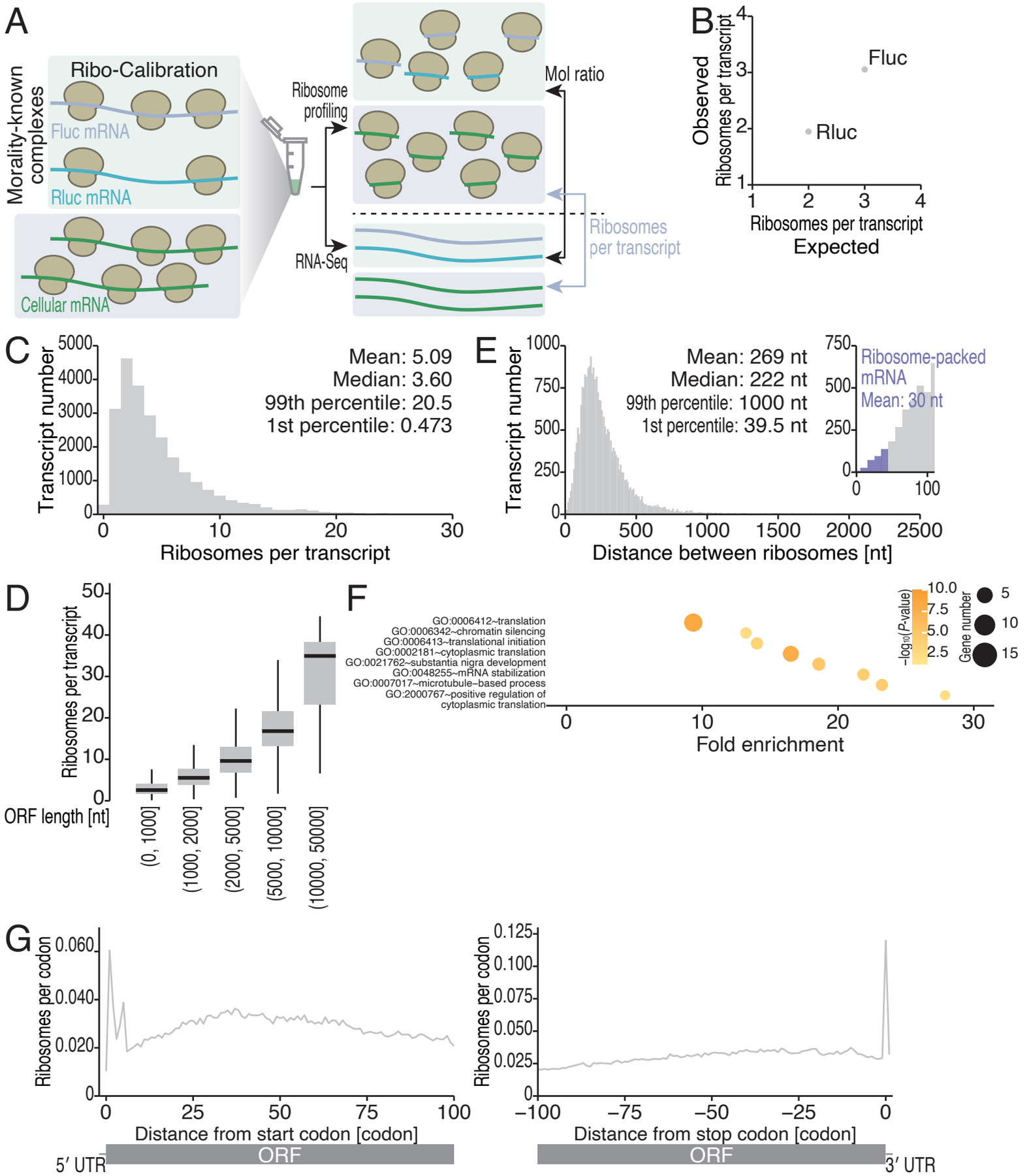

Figure 3 Tomuro, Mito *et al.* (2023)

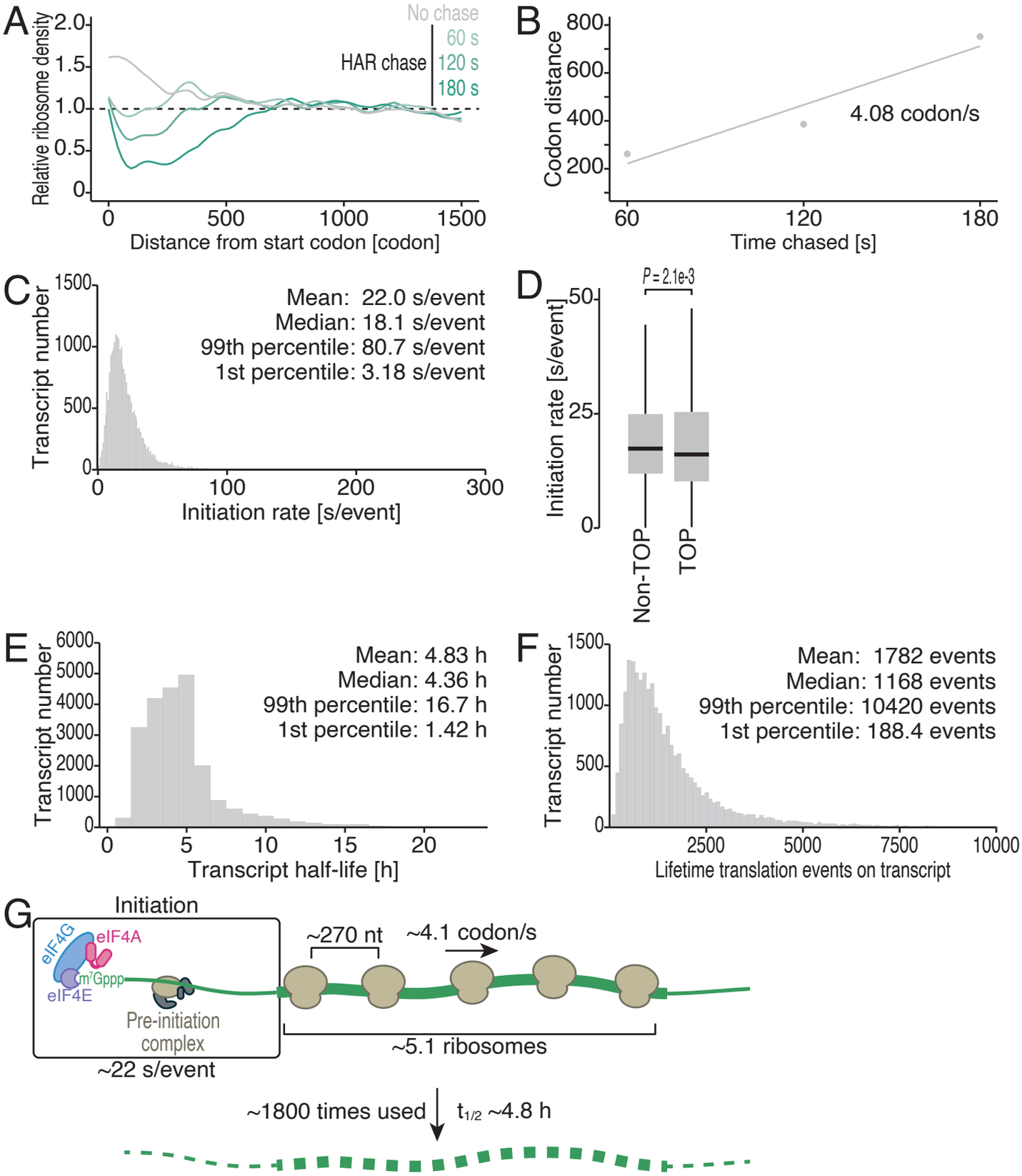

Figure 4 Tomuro, Mito *et al.* (2023)

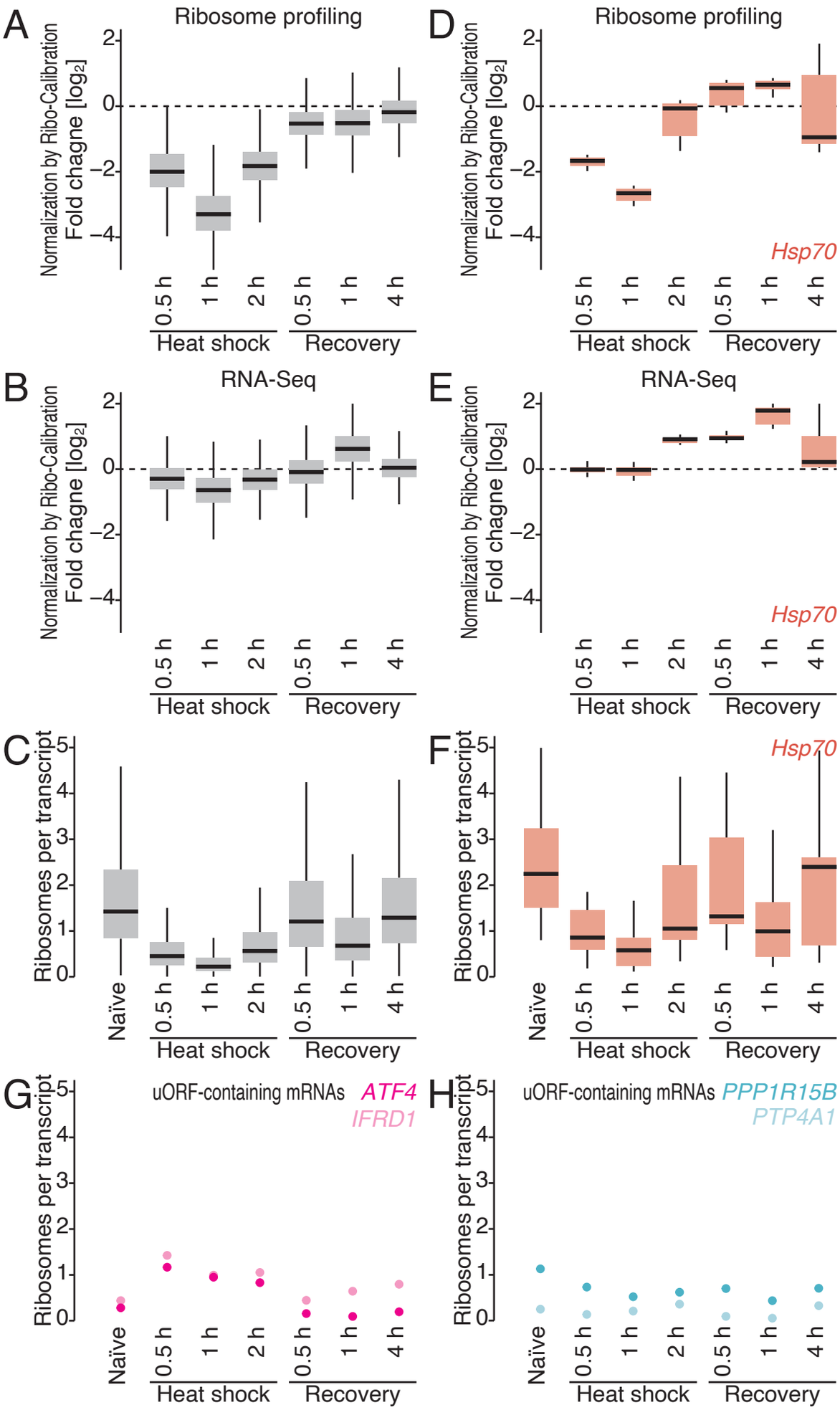

Figure 5 Tomuro, Mito *et al.* (2023)

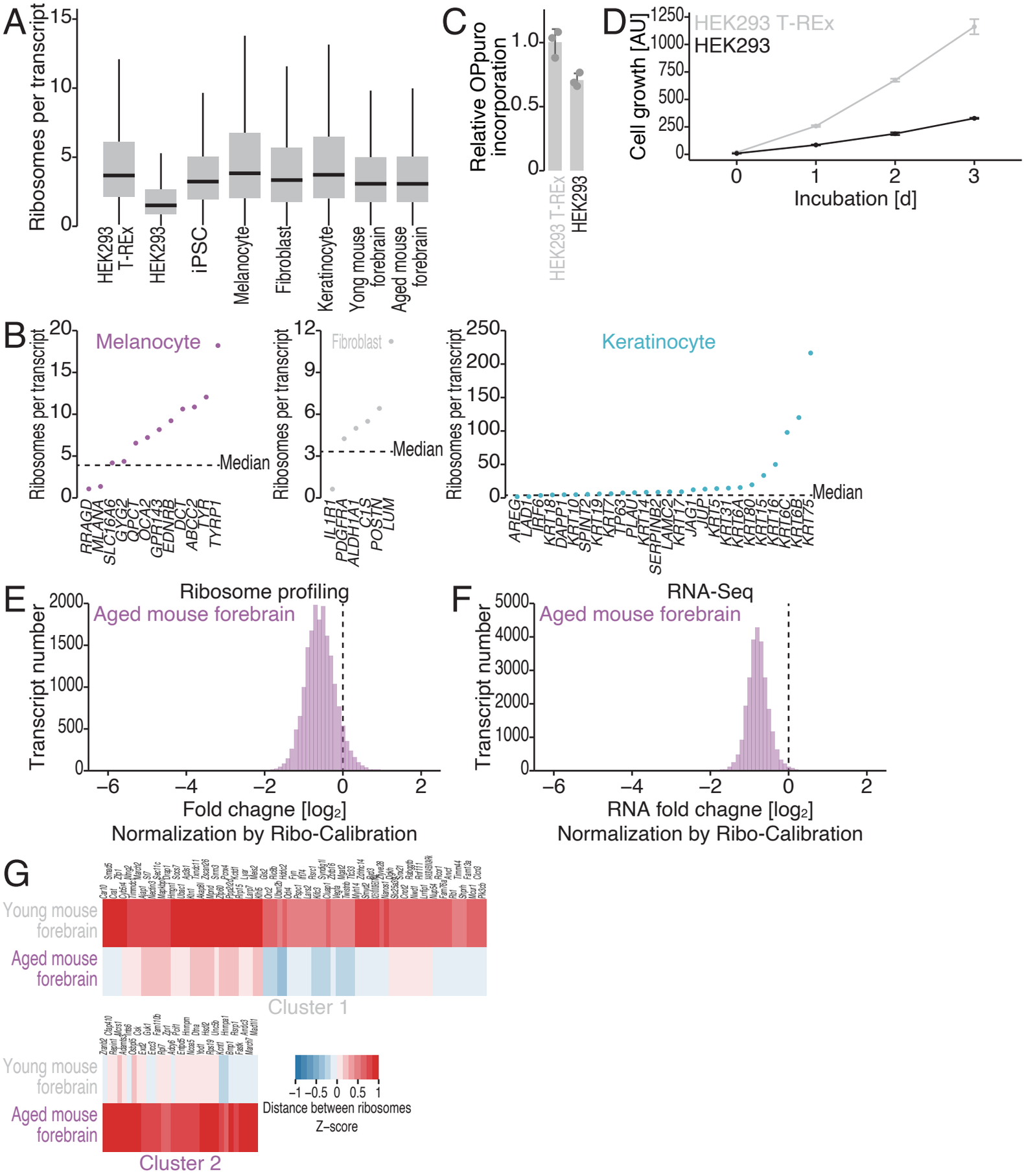

Figure 6 Tomuro, Mito *et al.* (2023)

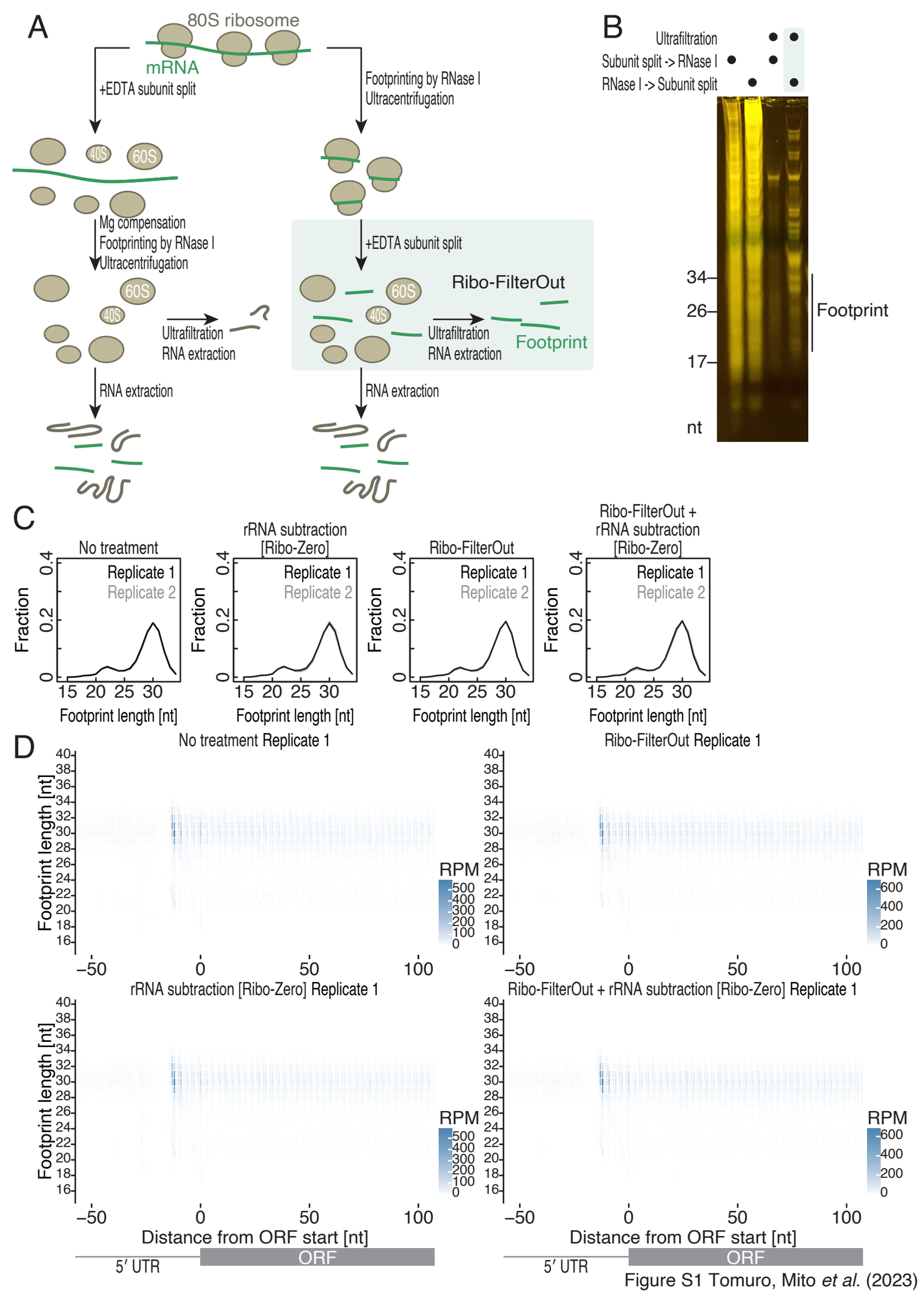

Figure S1 Tomuro, Mito *et al.* (2023)

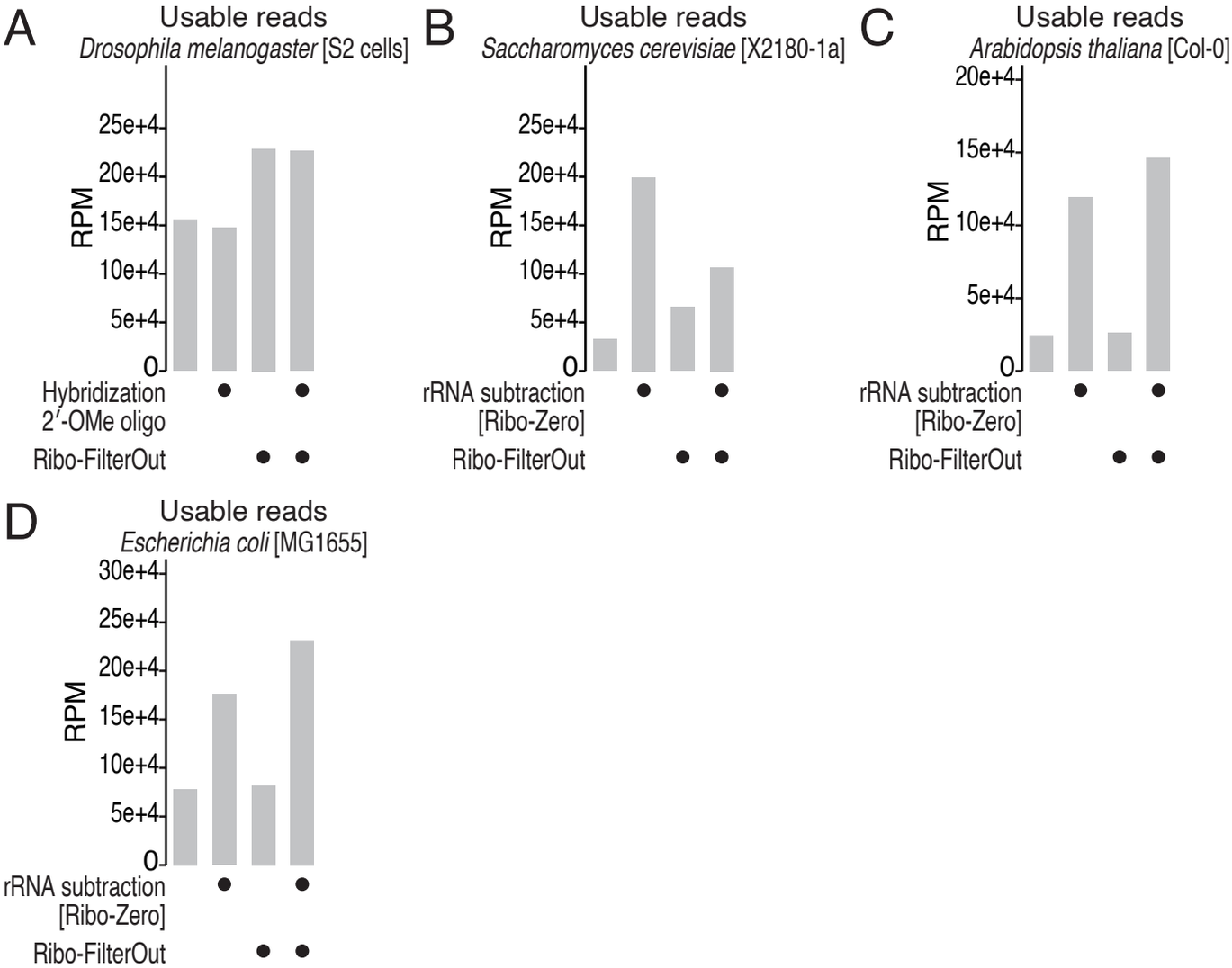

Figure S2 Tomuro, Mito *et al*. (2023)

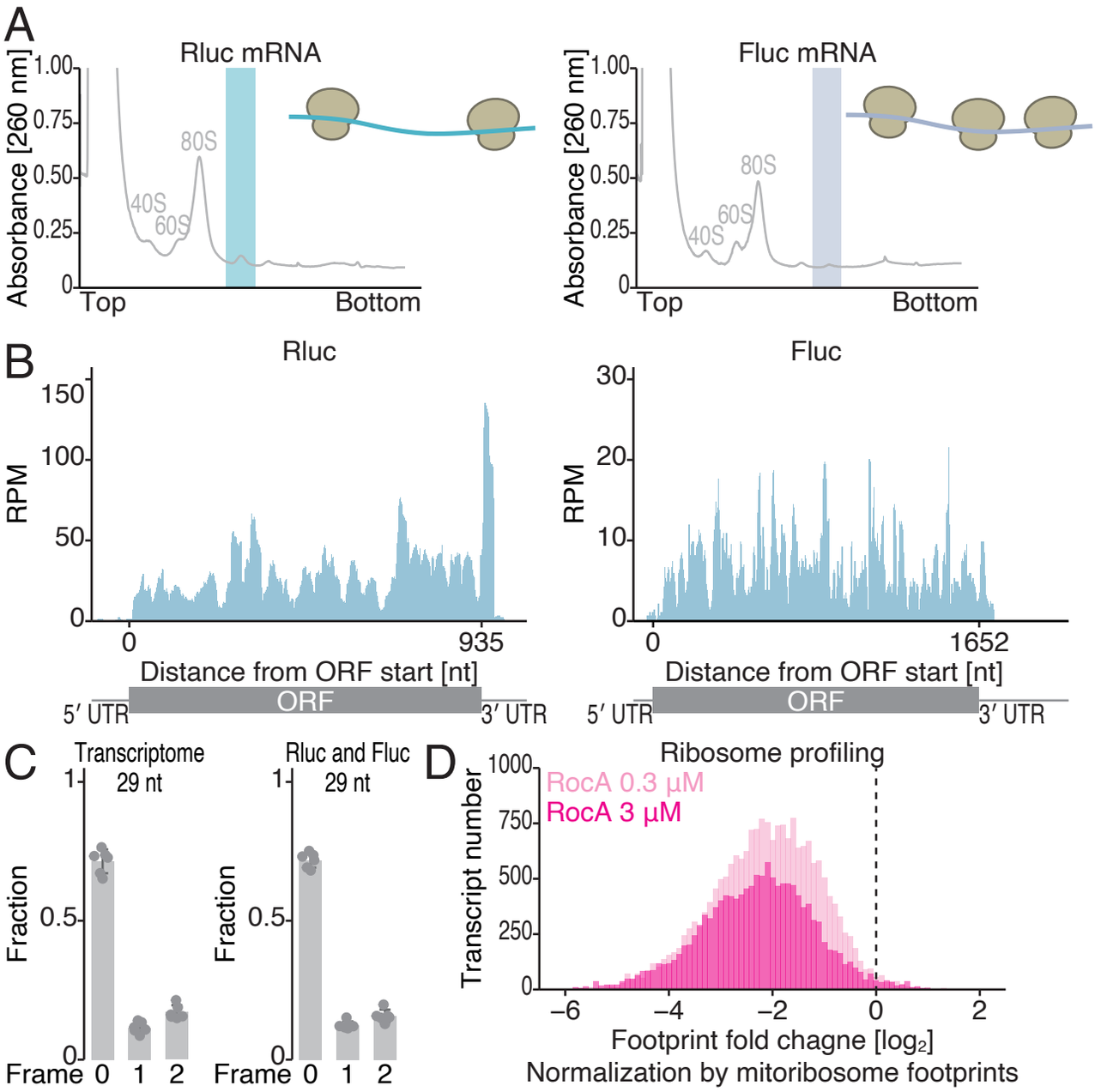

Figure S3 Tomuro, Mito *et al.* (2023)

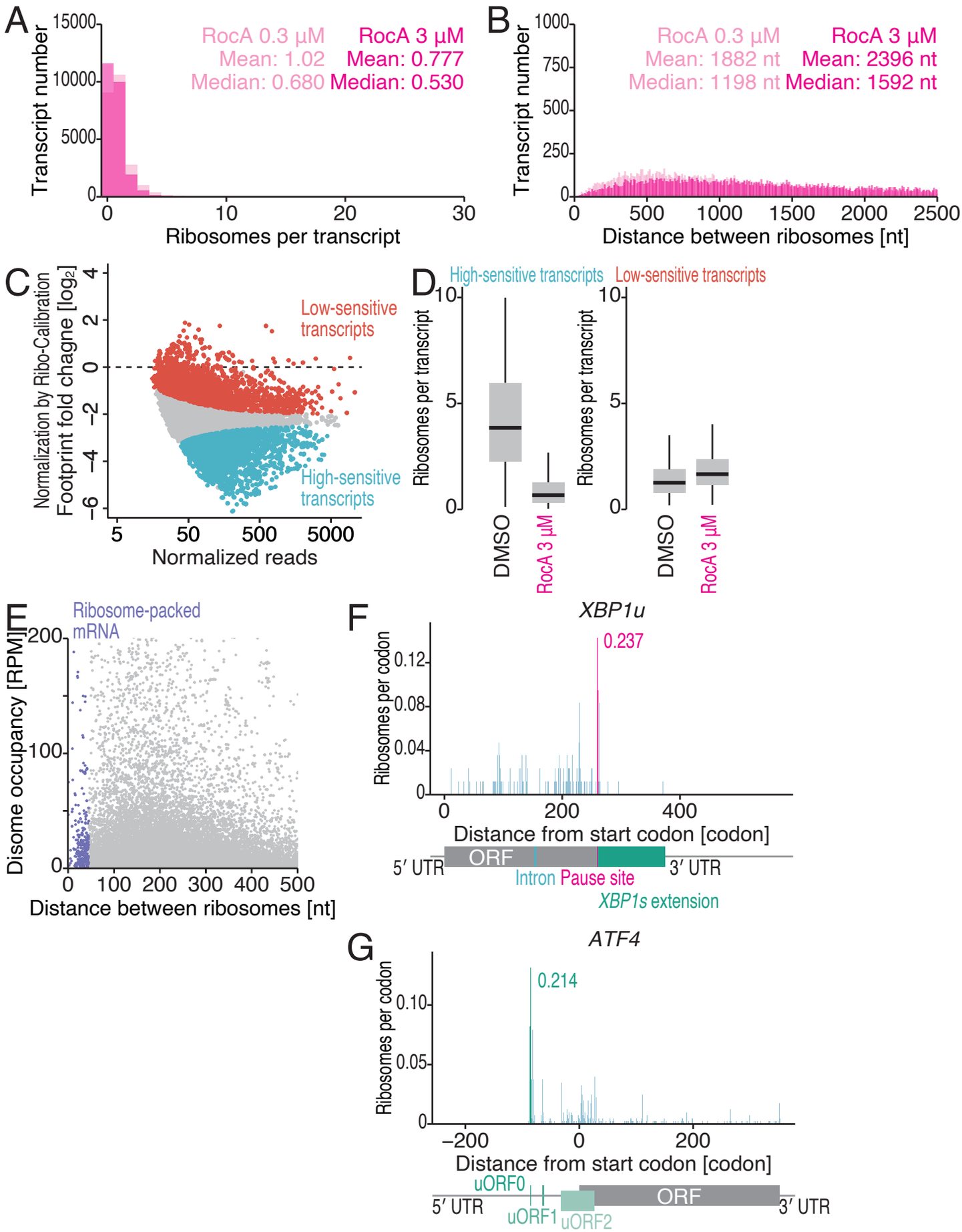

Figure S4 Tomuro, Mito *et al.* (2023)

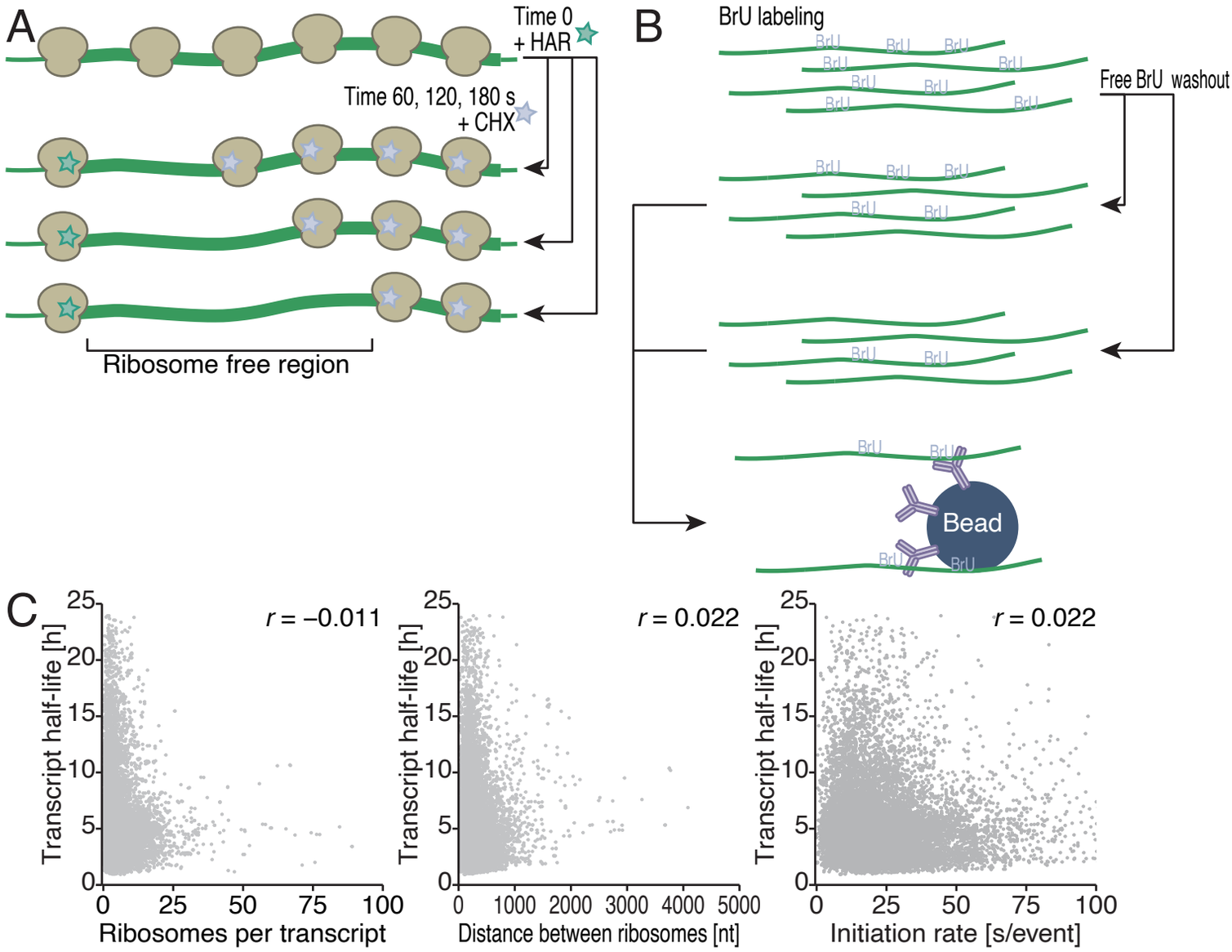

Figure S5 Tomuro, Mito *et al.* (2023)

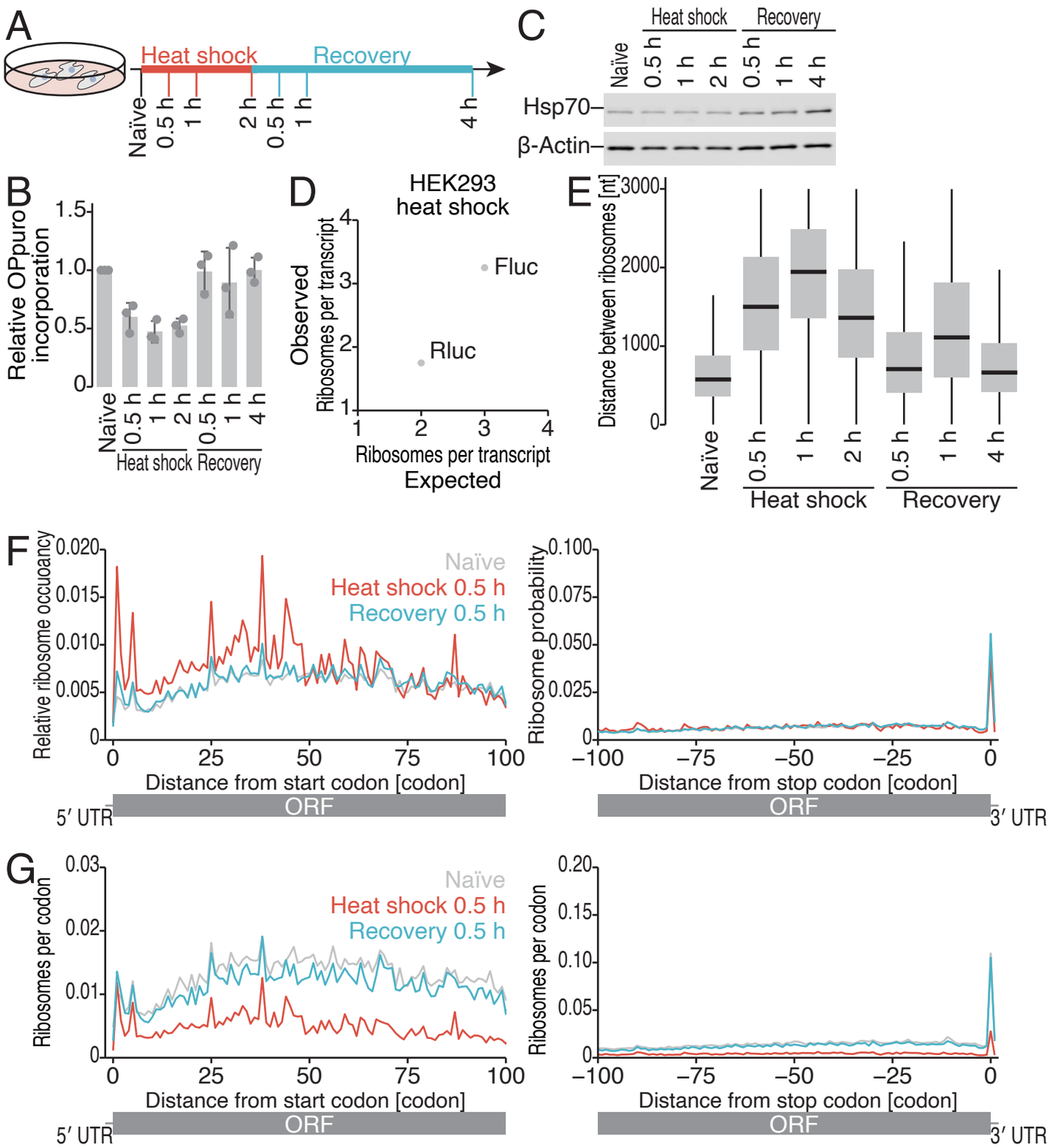

Figure S6 Tomuro, Mito *et al.* (2023)

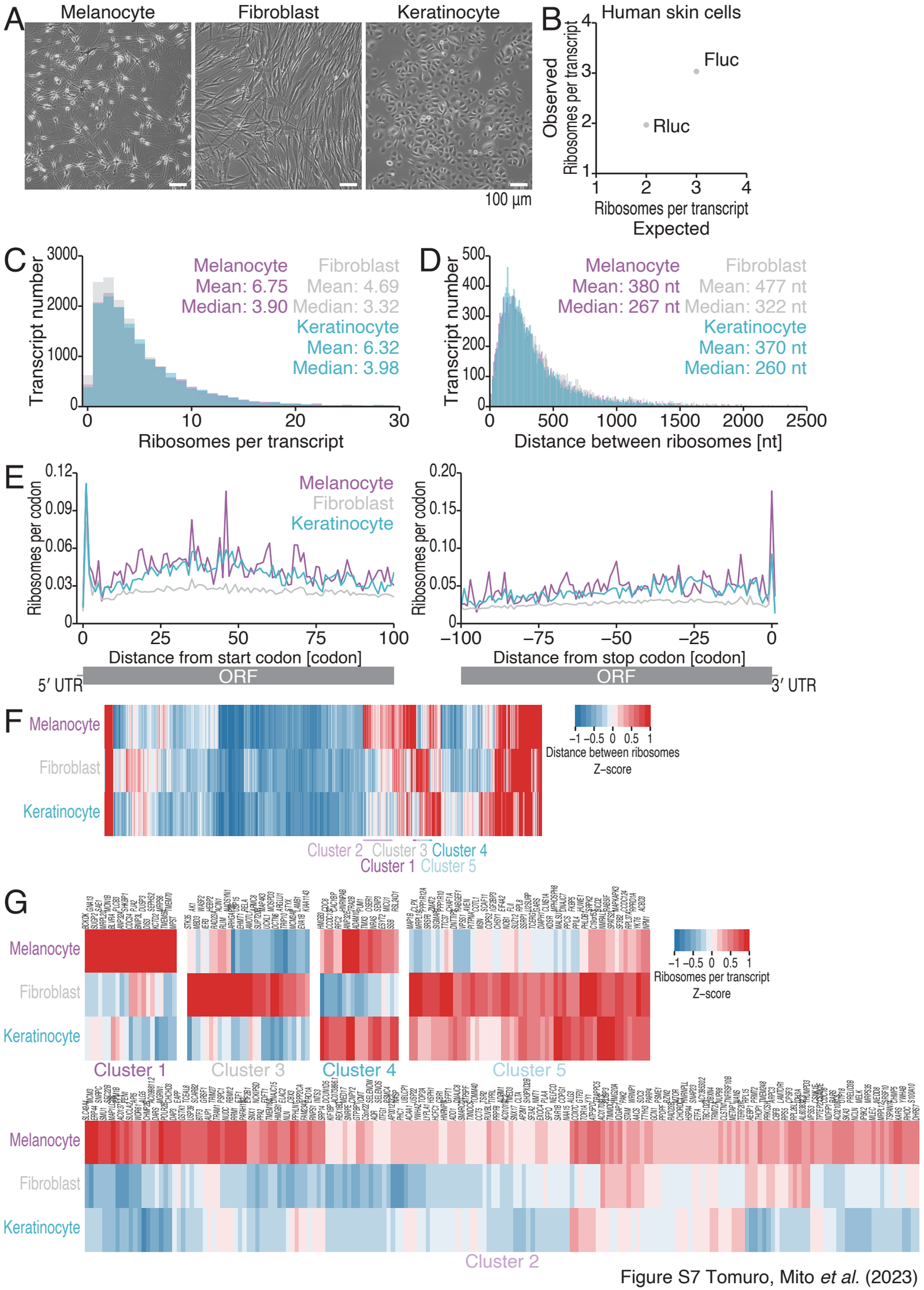

Figure S7 Tomuro, Mito *et al.* (2023)

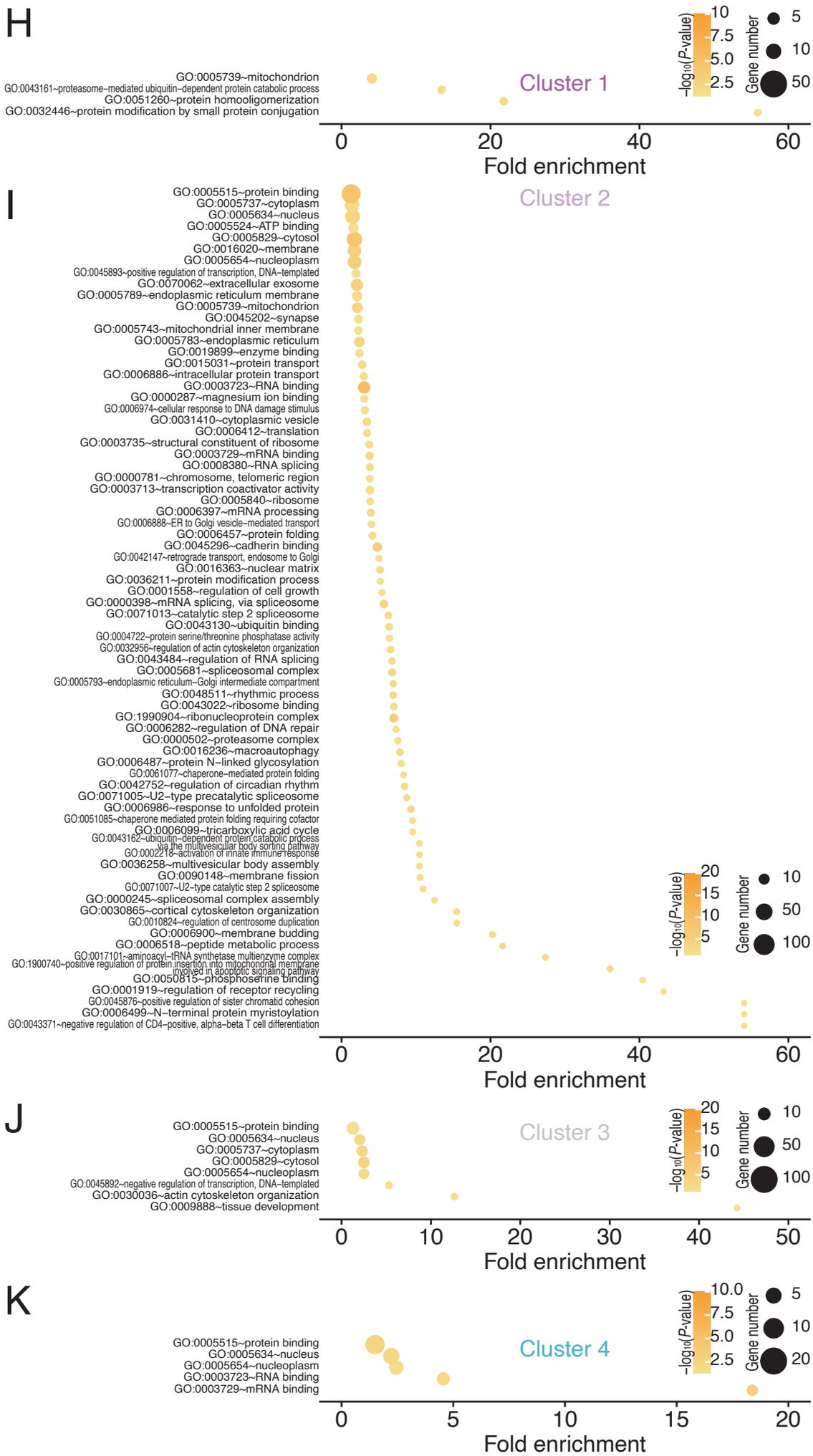

Figure S7 Tomuro, Mito *et al.* (2023)

L

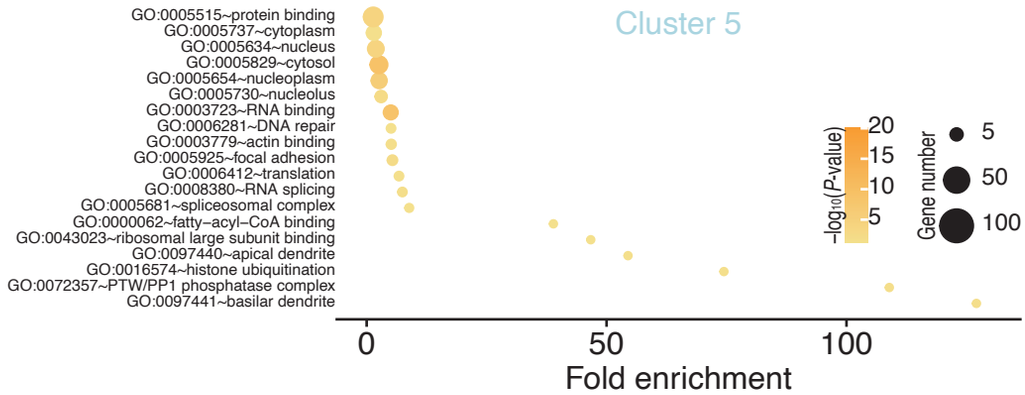

Figure S7 Tomuro, Mito *et al*. (2023)

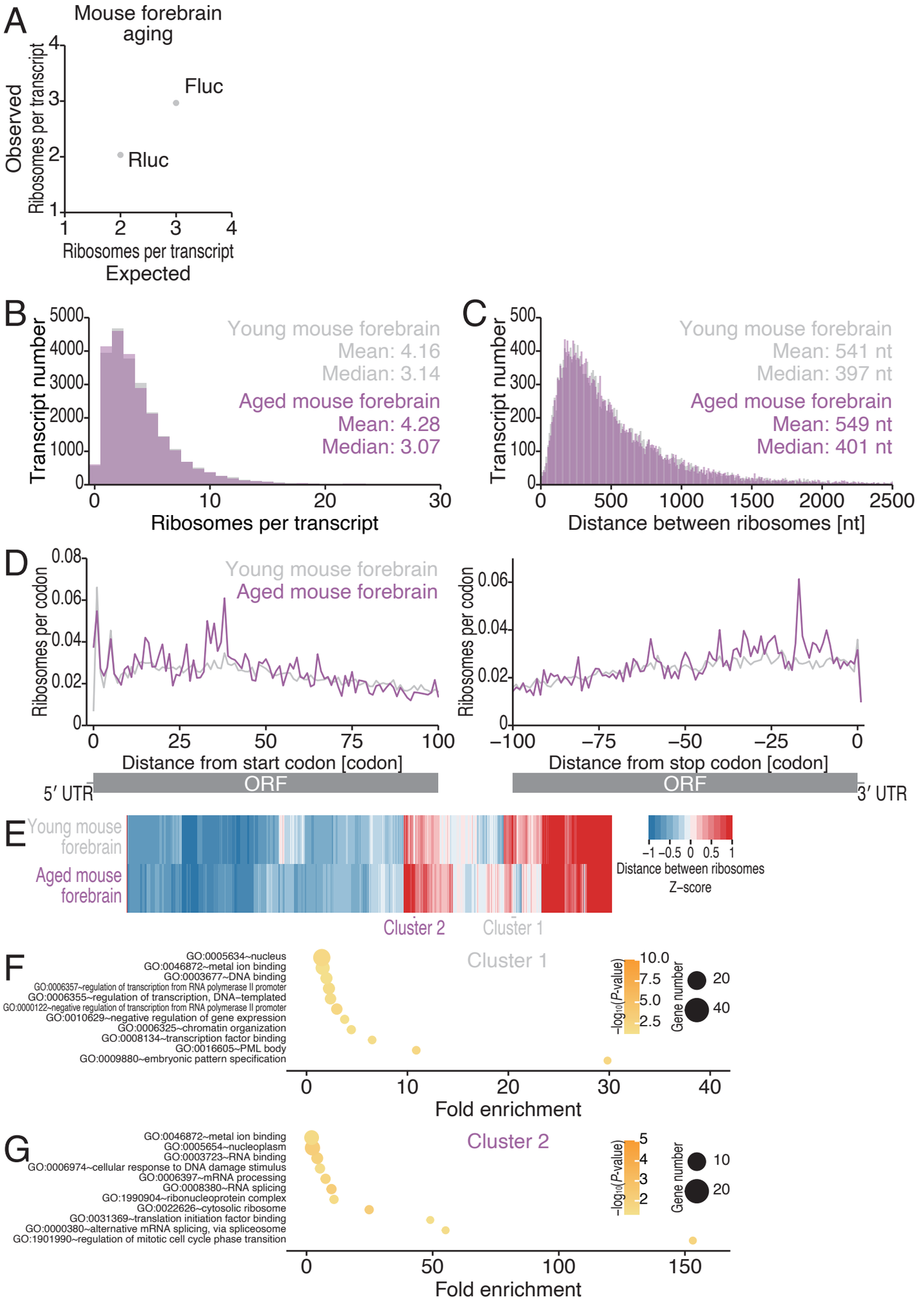

Figure S8 Tomuro, Mito *et al.* (2023)